# Turbulent Mixing in a Deep Fracture Zone on the Mid-Atlantic Ridge

LOUIS CLÉMENT AND ANDREAS M. THURNHERR

*Lamont-Doherty Earth Observatory, Columbia University, Palisades, New York*

LOUIS C. ST. LAURENT

*Woods Hole Oceanographic Institution, Woods Hole, Massachusetts*

(Manuscript received 5 December 2016, in final form 30 March 2017)

ABSTRACT

Midocean ridge fracture zones channel bottom waters in the eastern Brazil Basin in regions of intensified deep mixing. The mechanisms responsible for the deep turbulent mixing inside the numerous midocean fracture zones, whether affected by the local or the nonlocal canyon topography, are still subject to debate. To discriminate those mechanisms and to discern the canyon mean flow, two moorings sampled a deep canyon over and away from a sill/contraction. A 2-layer exchange flow, accelerated at the sill, transports 0.04–0.10-Sv ($1\,\mathrm{Sv} \equiv 10^6\,\mathrm{m^3\,s^{-1}}$) up canyon in the deep layer. At the sill, the dissipation rate of turbulent kinetic energy $\varepsilon$ increases as measured from microstructure profilers and as inferred from a parameterization of vertical kinetic energy. Cross-sill density and microstructure transects reveal an overflow potentially hydraulically controlled and modulated by fortnightly tides. During spring to neap tides, $\varepsilon$ varies from $O(10^{-9})$ to $O(10^{-10})\,\mathrm{W\,kg^{-1}}$ below 3500 m around the 2-layer interface. The detection of temperature overturns during tidal flow reversal, which almost fully opposes the deep up-canyon mean flow, confirms the canyon middepth enhancement of $\varepsilon$. The internal tide energy flux, particularly enhanced at the sill, compares with the lower-layer energy loss across the sill. Throughout the canyon away from the sill, near-inertial waves with downward-propagating energy dominate the internal wave field. The present study underlines the intricate pattern of the deep turbulent mixing affected by the mean flow, internal tides, and near-inertial waves.

## 1. Introduction

As part of the lower limb of the meridional overturning circulation, which is fundamental for Earth's climate, the formation of Antarctic Bottom Waters (AABW) has important effects on the climate, such as through the release of oceanic heat loss to the atmosphere (Talley 2013). In recent decades, a substantial portion of the atmospheric warming due to the anthropogenic greenhouse gases participated in the warming of abyssal waters (Purkey and Johnson 2010) via the formation of bottom waters. In spite of the primary role played by AABW in the circulation of physical and biogeochemical properties, their pathways and the processes giving rise to the turbulent diapycnal mixing providing the buoyancy flux that is required to close the AABW cell (Munk 1966) are still subject to significant uncertainty. For example, in the early theoretical model of the buoyancy-forced abyssal circulation (Stommel et al. 1958; Stommel and Arons 1960), the deep currents are driven by a uniformly distributed upwelling. In spite of the apparent importance of this vertical flow, the spatial distribution of the upwelling required to close the overturning circulation remains largely unknown. In the case of spatially uniform upwelling, the model of Stommel predicts poleward flow in the ocean interior to balance western boundary currents. Abyssal float data from the Brazil Basin in the western South Atlantic are fundamentally inconsistent with this prediction, however, and indicate a mean circulation dominated by meridionally and vertically interleaved zonal currents flowing in both directions (Hogg and Owens 1999; Thurnherr and Speer 2004). St. Laurent et al. (2001a) hypothesize that the observed zonal mean flows in the interior of the Brazil Basin are related to forcing by the high levels of mixing observed over the western flank of the Mid-Atlantic Ridge (MAR; Polzin et al. 1997).

Microstructure and tracer observations collected during the Brazil Basin Tracer Release Experiment

*Corresponding author*: Louis Clément, lclement@ldeo.columbia.edu

DOI: 10.1175/JPO-D-16-0264.1

(BBTRE) in the 1990s indicate high levels of turbulence and mixing over the topographically rough MAR flank (up to two orders higher diapycnal diffusivity on the MAR flank than over the adjacent abyssal plain). Early analyses of the BBTRE data (Polzin et al. 1997; Ledwell et al. 2000b; St. Laurent et al. 2001a) emphasize the hypothesis that the breaking of tidally forced internal waves generated over rough topography (Bell 1975) provides the energy for the elevated turbulence. The principal argument for a tidal energy source of the elevated mixing on the MAR flank is provided by an apparent spring–neap modulation of the near-bottom dissipation rate of turbulent kinetic energy $\varepsilon$ (Ledwell et al. 2000b; St. Laurent et al. 2001a). However, aliased sampling provides an alternative explanation for the observed variability in $\varepsilon$, as the BBTRE spring tide measurements were collected closer to the MAR crest, where turbulence levels are higher, than the neap tide measurements (Ledwell et al. 2000b; Toole 2007). To separate spatial from temporal patterns, a mooring was deployed in 1998 near 18°W inside a deep zonal canyon cutting across the MAR flank where the BBTRE tracer-release experiment was carried out (Ledwell et al. 2000b); we term this the BBTRE canyon.

A regional inverse model of the circulation on the western flank of the MAR near 20°S in the Brazil Basin based on the BBTRE microstructure and CTD data yields southwestward flow above the topography (St. Laurent et al. 2001a), consistent with float trajectories (Hogg and Owens 1999) and tracer advection (Ledwell et al. 2000a). The model also shows bottom water flowing eastward toward the MAR crest in the fracture zone (FZ) canyons, which corrugate almost the entire flanks of slow-spreading midocean ridges, including the MAR flank in the Brazil Basin (St. Laurent et al. 2001a). In the data of the model inversion, turbulence levels are significantly higher below the topographic peaks (i.e., within the FZ canyons) than above the ''topographic envelope'' (Fig. 3 in St. Laurent et al. 2001b). A steady-state heat budget of the BBTRE canyon indicates that the primary balance is between along-canyon advection and vertical eddy diffusion (St. Laurent et al. 2001b), similar to the situation in other sloping submarine valleys (Thurnherr et al. 2002).

The velocity data from the BBTRE mooring are qualitatively consistent with this heat budget, although they indicate mean up-canyon velocities of several centimeters per second (Thurnherr et al. 2005), nearly an order of magnitude above the heat budget–derived estimates. Thurnherr et al. (2005) interpret this discrepancy between the modeled and observed up-canyon velocities as evidence that mixing hotspots were insufficiently sampled during BBTRE. They suggest turbulence associated with hydraulic overflows across sills on the canyon floor as a hypothesized source of the ''missing mixing'' because of a strong association between the presence of sills between two hydrographic stations and the corresponding along-canyon density gradients. Overflow processes contribute significantly to the transformation of deep-water masses within narrow interbasin passages (Polzin et al. 1996; Mercier and Morin 1997; Ferron et al. 1998). The role of such passages is particularly relevant in the Brazil Basin, which, for AABW, is connected to other ocean basins via five confined channels (Hogg et al. 1996). Similarly, interbasin passages are known to affect the transformation of deep-water masses in the Pacific (Alford et al. 2013; Voet et al. 2015) and Indian Oceans (MacKinnon et al. 2008). The BBTRE canyon is not an interbasin passage, however, as it terminates at the MAR crest (Thurnherr et al. 2005). Even in such enclosed submarine valleys, hydraulic overflows are common (Thurnherr and Richards 2001; Thurnherr et al. 2002, 2008) and associated with high levels of turbulence and mixing (St. Laurent and Thurnherr 2007; Tippenhauer et al. 2015). Most overflows in the ocean display signs of hydraulic control (Turner 1973); the velocities increase greatly as the flow approaches the sill (or constriction) and accelerate for some distance downstream before returning to upstream levels fairly abruptly. Overflow processes known to be associated with high levels of turbulence include shear instabilities along the interface between the fast-flowing part of the overflow and the overlying water column as well as hydraulic jumps (Wesson and Gregg 1994). Additionally over shallower sills, the tidal modulation of internal hydraulic control was recognized in fjords (Farmer and Smith 1980; Staalstrøm et al. 2015) and in interbasin passages (Wesson and Gregg 1994); some of the barotropic tidal energy can radiate away as internal waves (Klymak and Gregg 2004) and affect the far-field turbulence in the ocean. Internal wave trapping (Gordon and Marshall 1976) can further intensify canyon mixing (Kunze et al. 2002; Carter and Gregg 2002) in the BBTRE canyon, where near-inertial waves are known to modulate the shear variance (Toole 2007).

With the Dynamics of Mid-Ocean Ridge Experiment (DoMORE) project, we aim to study the role of overflow processes in a 200-km-long section of the BBTRE canyon that includes the largest along-canyon density drop and turbulence levels (Thurnherr et al. 2005). Using data from hydrographic surveys and from several moorings, we study the influence of a large overflow on a 2-layer exchange mean flow and on along-canyon density gradients (section 3a). The spatial variability of the dissipation rate and its tidal dependence at the sill and away from it are investigated (section 3b). The survey

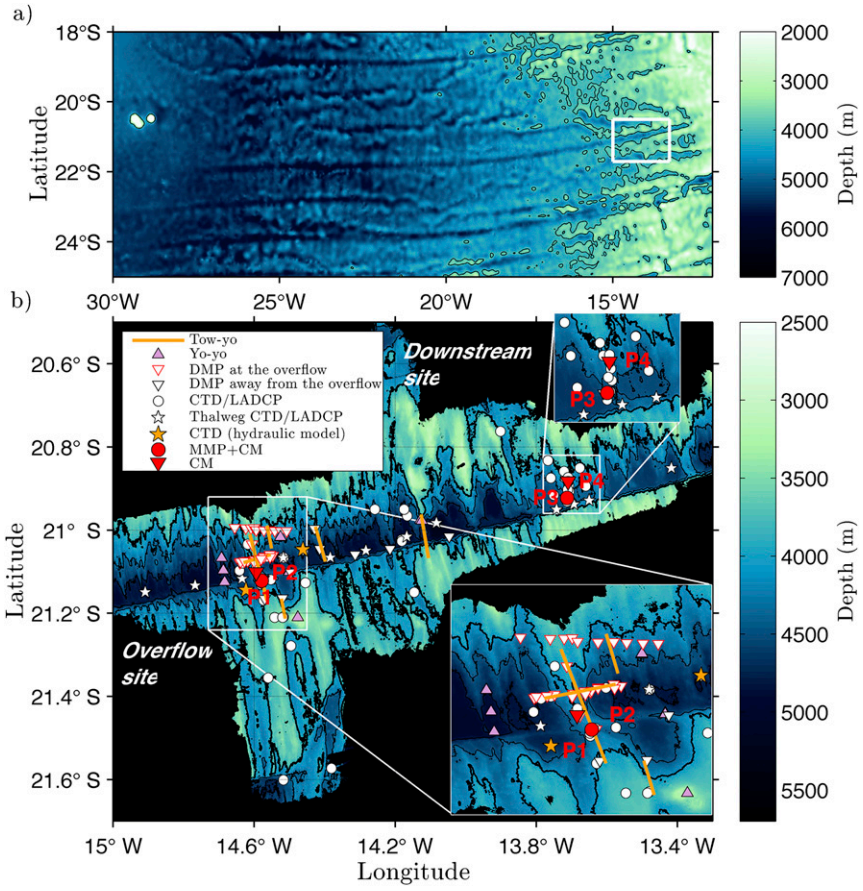


FIG. 1. (a) Bathymetry in the South Atlantic of a midlatitudinal section on the western flank of the Mid-Atlantic Ridge and (b) over a fracture zone canyon around 21°S. (top) The 3900 m and (bottom) the 3900-, 4300-, and 4700-m isobaths are contoured. The insets display the topography over two sites (the overflow and downstream sites) with along- and across-sill tow-yo transects (orange lines), yo-yos (purple triangles), and CTD/LADCP profiles (black circles and stars), associated with DMP profiles (red and black triangles) and four moorings distributed with current meters (red triangles), two of which contain MMPs (red circles).

suggests the occurrence of an overflow with enhanced downstream turbulence fortnightly modulated at the sill (section 3c). The moorings detect overturns (section 3d) and inform on the finestructure properties of internal waves (section 3e) at two locations: at the sill (mooring P1) and away from any topographic features (mooring P3). Consistent with the microstructure survey, large turbulent overturns around the 2-layer interface are phase locked with semidiurnal tides at spring tides at P1, reminiscent of a forming internal lee wave during slacking tides. Away from the sill, finestructure characteristics support the predominance of near-inertial waves with downward-propagating energy. In section 4, we quantify the dissipation rate at the sill and the energy radiated by internal waves, which both potentially contribute to remove the across-sill energy of the lower layer and of the barotropic tides.

## 2. Data and methods

### *a. Study region*

As is the case for most of the slow-spreading mid-ocean ridges, the western flank of the MAR in the Brazil Basin is corrugated by FZ canyons, which are typically between 500 and 1000 m deep and spaced approximately 50 km apart (Tucholke and Lin 1994). For the DoMORE project, an ≈170-km-long stretch of one of these FZ canyons, the BBTRE canyon, was chosen (Fig. 1) to include both the location with the largest along-canyon density gradient near 14.6°W, where Thurnherr et al. (2005) inferred the existence of a major overflow as well as ≈100 km of canyon downstream from this overflow where the along-canyon density gradient observed during BBTRE was reduced compared with the gradient at 14.6°W. Along its axis, the BBTRE canyon is corrugated

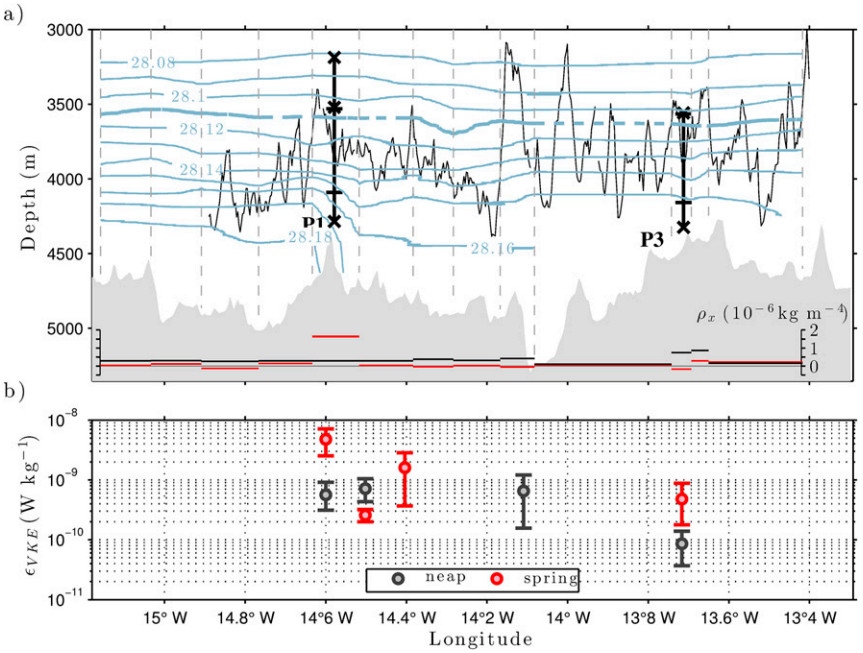


FIG. 2. (a) Along-canyon isopycnals $\gamma_n$ with the main sill located at 14.6°W. The thalweg (gray) and the canyon rim of the northern wall with a mean depth of 3860 m (black) are displayed. The isopycnal at the deep-water mass separation of AABW/LNADW ($\gamma_n$ = 28.11) is indicated (thick). The along-canyon gradient of density $\rho_x$ averaged in the bottommost 50 m above any intrusion of the thalweg is displayed below each station pair (red) as well as the density gradient uncertainty (black); $\rho_x$ positive corresponds to decreasing density toward the MAR. (b) Turbulent dissipation rate estimated from the VKE $\varepsilon_{\mathrm{VKE}}$ inferred from LADCP profiles during two spring–neap cycles and averaged every 0.1° of longitude for the spring (red) and neap (black) tidal periods and integrated in height above bottom to 1000 m. The 95% confidence intervals are indicated based on bootstrapping.

by meridionally elongated spanwise topographic structures that are called bathymetric hills and that form both sills and constrictions for any deep along-canyon flow (Fig. 1b). In terms of first-order topography (canyon width and depth, presence of topographic hills) as well as hydrography (along-canyon density gradients and stratification), the BBTRE canyon is similar to many other FZ canyons in the South Atlantic (Thurnherr and Speer 2003).

Over most of the DoMORE study region, the bathymetric hills are much more prominent along the northern canyon wall, which is considerably less steep than the southern sidewall, especially east of 14.2°W (Figs. 1b, 3c). A well-defined break in cross-canyon steepness along the southern wall is used to define a nominal canyon wall depth of 3900 m. The topographic data are acquired by a Kongsberg EM122 multibeam echo sounder with a horizontal resolution of 50 m and merged with the previous BBTRE survey (Ledwell et al. 2000a). Those data reveal deeper connections between the BBTRE canyon and its northern and southern neighbor canyons near 13.8° and 14.6°W, respectively (Fig. 1b). The average width of the BBTRE canyon in the DoMORE study region along the 3900-m isobath is ≈18 km. The maximum depth at each longitude is used to define the mean depth along the thalweg of ≈4760 m for the DoMORE study region. The BBTRE canyon reaches both its minimum width (≈10 km) and axial depth (≈4290 m) in the saddle of a particularly tall bathymetric hill near 14.6°W (Fig. 2). The basins on each side of the resulting sill are ≈4700 m deep; the estimated length of this sill is ≈8 km. At the sill, the topography is closed below 4000 m except for a 2-km-wide deep passage (Fig. 3a).

### b. Measurements

The BBTRE canyon region was visited twice with the R/V *Nathaniel B. Palmer* for the DoMORE project. During the first cruise (DM1) in July 2014, a topographic survey was carried out, lowered acoustic Doppler current profiler (LADCP) and conductivity–temperature–depth (CTD) profiles were collected (a combination of full-depth profiles and tow-yo and yo-yo casts), and an array of moored instruments was deployed. During the second cruise (DM2) in October 2015, the moored instruments were recovered, additional LADCP/CTD data were collected, and 41 microstructure casts were

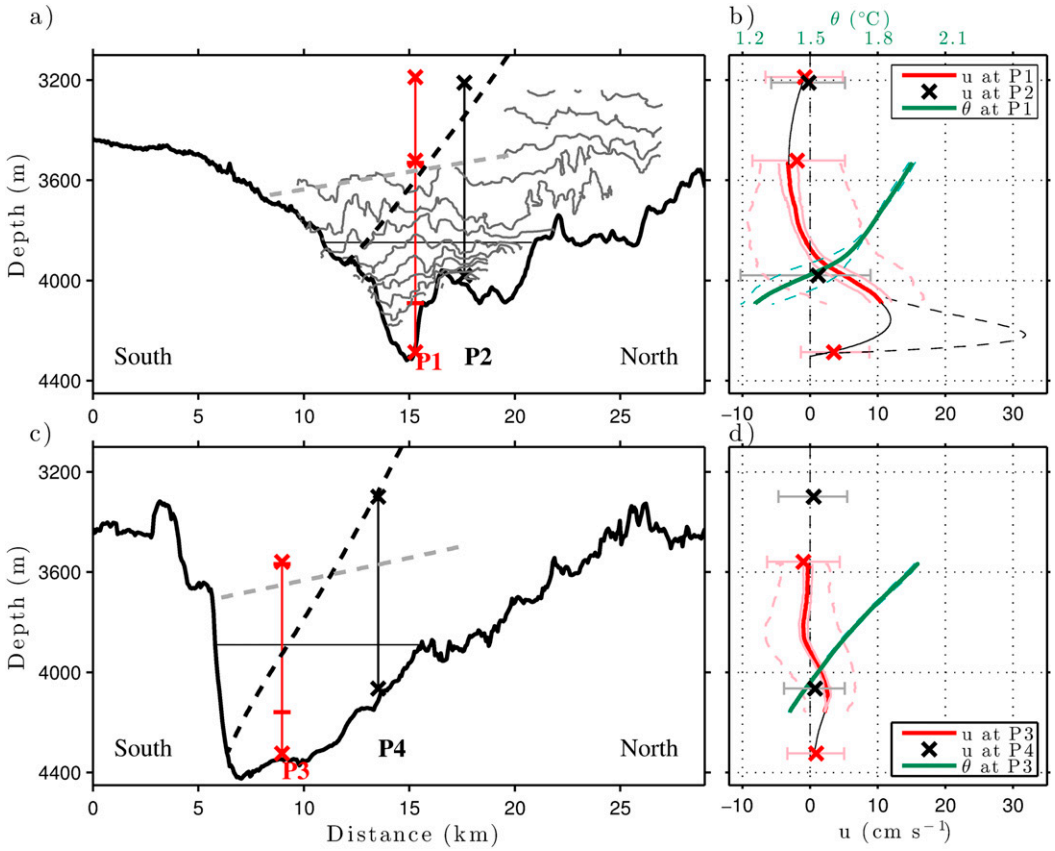


FIG. 3. Topography of the cross-canyon sections (a) at the overflow site around the sill (moorings P1 and P2) with isopycnals from one tow-yo transect and (c) at the downstream site located 100 km eastward from the sill (P3 and P4). The current meter depths are indicated (crosses) as well as the MMP limits at P1 and P3 (thick lines). The ray paths are displayed for semidiurnal (dashed black) and near-inertial waves (dashed gray). Mean (thick red), standard error (pink), and 10th percentiles (dashed pink) of the zonal velocity (b) at the overflow site and (d) at the downstream site measured from the MMP and from the current meters (crosses, with the 10th percentiles error bars). A polynomial fit is applied on the temporal mean of MMP and current meter velocities (thin black), whereas another fit is applied on one LADCP profile (thin dashed black) taken within the sill passage in (b). The mean (green) and corresponding 10th percentiles of temperature (dashed green) at P1 and P3 are added in (b) and (d), respectively.

carried out with a deep microstructure profiler (DMP). The moorings were deployed at the location of the minimum canyon cross section near 14.6°W (overflow site) as well as in a similarly shallow area ≈100 km farther east (downstream site; Figs. 1–3), and most hydrographic profiles were collected between these two mooring sites. A total of 58 and 66 full-depth LADCP/CTD pairs were collected during DM1 and DM2, respectively; at 41 of the DM2 stations, simultaneous profiles of microstructure were collected as well. In addition to those full-depth pairs, 215 (140 and 75 for DM1 and DM2, respectively) partial-depth LADCP/CTD pairs below 3000 m were collected during several tow-yo transects both across the sill at the overflow site and meridionally across the BBTRE canyon at several locations (Fig. 1).

Temperature and salinity profiles were collected with a SBE 911plus CTD mounted on a SBE32 rosette using a wire speed of 50 m min$^{-1}$. The tow-yo casts were collected with a mean vessel speed of 0.6 knots (1 knot = 0.51 m s$^{-1}$); the package location was estimated from the ship's location, wire out, and altimetry data. All CTD sensors were precruise calibrated, and there are no indications for significant drifts in any of the sensor data. The temperature uncertainty provided by the manufacturer is ±0.001°C. An accuracy of 0.001 for salinity is estimated from the results of salinometer calibrations using a Guildline Portasal SA10 for both cruises.

Velocity profiles were collected with upward- and downward-facing Teledyne RDI Workhorse ADCPs mounted on the rosette. Horizontal velocities are calculated with the LDEO_IX implementation of the

TABLE 1. Mooring locations at the overflow site (P1 and P2) and at the downstream site (P3 and P4) with each instrument (MMP and Nortek Aquadopp), depth, start, and end dates. The DoMORE surveys (DM1 and DM2) are indicated.

| Mooring | Position | Instrument | Measurement | Depth (m) | Start date | End date |
|---|---|---|---|---|---|---|
| P1 | 21.12°S, 14.58°W | Nortek Aquadopp (P1c/P1b/P1a) | $u, v$ | 3188/3521/4285 | 21 Jul 2014 | 25 Aug 2015 |
| | | MMP | $u, v, S, T, P$ | 3530–4094 | 22 Jul 2014 | 21 Mar 2015 |
| P2 | 21.10°S, 14.59°W | Nortek Aquadopp (P2b/P2a) | $u, v$ | 3210/3979 | 22 Jul 2014 | 21 Sep 2015 |
| P3 | 20.92°S, 13.71°W | Nortek Aquadopp (P3b/P3a) | $u, v$ | 3559/4324 | 26 Jul 2014 | 22 Sep 2015 |
| | | MMP | $u, v, S, T, P$ | 3567–4159 | 27 Jul 2014 | 27 May 2015 |
| P4 | 20.88°S, 13.71°W | Nortek Aquadopp (P4b/P4a) | $u, v$ | 3299/4064 | 27 Jul 2014 | 22 Sep 2015 |

| Survey | Instrument | Measurement | Number of profiles (middepth) | Start date | End date |
|---|---|---|---|---|---|
| DM1 | CTD/LADCP | $S, T, P/u, v$ | 58 (140) | 10 Jul 2014 | 29 Jul 2014 |
| DM2 | CTD/LADCP | $S, T, P/u, v$ | 66 (75) | 20 Sep 2015 | 7 Oct 2015 |
| | DMP | $\varepsilon$ | 41 | | |

velocity inversion method (Visbeck 2002). Most of the DM1 LADCP profiles were collected with two 300-kHz instruments; during DM2 a downward-facing, 150-kHz ADCP was used together with an upward-facing, 300-kHz instrument. Because of weak acoustic backscatter, different bin sizes and blanking distances were tried; most of the profiles used here were collected with pulse and bin lengths of 32 and 16 m, respectively. LADCP data quality is assessed by comparing the upper-ocean horizontal velocities derived without the shipboard ADCP (SADCP) constraint to the corresponding SADCP velocities; based on data from many different regions, typical rms discrepancies for high-quality LADCP datasets are 4–6 cm $s^{-1}$. Extremely weak acoustic backscatter in the DoMORE study region resulted in many LADCP profiles of insufficient or questionable quality. The horizontal LADCP velocities used here are all taken either from bottom-track solutions near the seabed (where acoustic backscatter is significantly greater than in the midwater column) or from profiles that passed careful visual inspection and using a 6 cm $s^{-1}$ threshold for the rms LADCP–SADCP velocity difference. In addition to the horizontal velocities, the DoMORE LADCP data are also processed for vertical velocity (Thurnherr 2011). Because of the weak acoustic backscatter, the vertical velocities were processed in 40-m bins.

We used a Rockland VMP-6000 (RVMP), manufactured by Rockland Scientific International, Inc., to obtain profiles of microstructure from which $\varepsilon$ is derived. Details of the RVMP instrument system can be found online (at http://www.rocklandscientific.com). The RVMP measures centimeter-scale shear of velocity $u$ with depth $z$ using airfoil probes, from which the dissipation rate of turbulent kinetic energy is estimated as $\varepsilon = (15/2)\nu\langle(du/dz)^2\rangle$ (appendix A), where $\nu$ is the molecular viscosity of seawater and $\langle\cdot\rangle$ is the integrated vertical wavenumber spectra. Here, we have invoked isotropy relations (Hinze 1975) to reduce the 9-component rate of strain tensor to a single microscale shear component.

Four moorings (Fig. 3; Table 1) recorded the mean flow, tides, and near-inertial waves at the overflow and downstream sites. Two McLane moored profilers (MMP), each equipped with an acoustic current meter (ACM) and a CTD from Falmouth Scientific, Inc., sampled the water column between ≈200 and 800 mab, crawling up and down the wire at approximately 25 cm $s^{-1}$: P1 in the sill saddle at the overflow site (21.12°S, 14.58°W) and P3 in the deepest part of the canyon at the downstream site (20.92°S, 13.71°W), located ≈100 km east of P1. Both MMPs collected three, consecutive, 90-min-long temperature, salinity, and horizontal velocity profiles once every half-inertial period (16.7 h) concurrently during 8–10 months. ACM postprocessing includes compass calibration (Toole et al. 1999) and subsampling on a 2-dbar pressure grid. The accuracy of the derived velocity data is in the cm $s^{-1}$ range (J. Toole 2016, personal communication), whereas the random noise of the raw path velocities mostly attributed to the instrument vibration is of ~1 cm $s^{-1}$ (Doherty et al. 1999). Outliers above three median absolute deviations of the 0.05-Hz high-pass filtered conductivity, temperature, and pressure sampled at 2 Hz are replaced by the median over three consecutive points. A recursive filter (Mudge and Lueck 1994) is applied on the conductivity and pressure to minimize the effect of salinity spikes on the density. Each mooring had a Nortek Aquadopp acoustic current meter sampling the velocities every 10-min ≈10 m above the seabed as well as another instrument near the top of the MMP profile turnaround; on mooring P1, an additional current meter recorded the velocities near 3200 m. Both at the overflow

and downstream sites, there were additional moorings (P2 and P4, respectively) with Aquadopp current meters both near the seabed and ≈800 m up in the water column; partway up on the northern canyon walls (Fig. 3).

The barotropic tidal velocities from the 1/4° TPXO7.2 tidal model (Egbert and Erofeeva 2002) are used to establish the phase of the spring–neap cycle at P1 and P3 and the phase of the semidiurnal tides at P1. A harmonics analysis (Pawlowicz et al. 2002) was conducted at P1c (at 3200 m, above the canyon walls) and at P3b (at 3600 m) with data from the shallowest current meters to reduce the effects of the baroclinic current arising from the local topography. The Greenwich phases of the $M_2$ and $S_2$ TPXO components (at the location of P1) are 131.63° ± 0.02° and 147.46° ± 0.05°, whereas they are 146.4° ± 3.9° and 155.1° ± 6.1° from the current meter at P1c; a lag of ~30 min is observed with the $M_2$ tidal predictions. In addition, the observed $M_2$ and $S_2$ phases at P3b (149.8° ± 3.9° and 163.1° ± 14.8°) do not significantly differ from P1c. As such, we refer to the TPXO tides at P1 to distinguish the spring and neap tides in the DoMORE surveys and for each mooring. The spring tides with a period of $dt$ = 14.79 days $[1/(\omega_{S_2}+\omega_{M_2})]$ are selected from the maximum of the hourly TPXO $S_2 + M_2$ tidal predictions during the first month sampled by mooring P1 and then by adding $dt$ to the remaining sampled period. The $M_2$ amplitude (semimajor axis) of the TPXO barotropic tide (3.08 ± 0.01 cm s$^{-1}$) agrees with the harmonic analysis at P1c (3.2 ± 0.1 cm s$^{-1}$) and at P3b (3.0 ± 0.1 cm s$^{-1}$).

### c. Derived parameters

Based on an empirical link between the Ozmidov and the Thorpe scales, the length scale of density overturns can be related to patches of active turbulence (Thorpe 1977; Dillon 1982). The Ozmidov scale $L_O$ is the upper limit of the size of isotropic overturns in a stratified fluid. The Thorpe scale $L_T$ defines a vertical size of turbulent overturns from the root-mean-square of Thorpe displacement $d'$, estimated from the difference between the reordered gravitationally stable and observed density profile. The Thorpe scale has been shown to be highly correlated with the Ozmidov scale under conditions of internal wave–driven overturns in the well-stratified thermocline with $L_O = a\langle(d')^2\rangle^{1/2}$, where angle brackets indicate an average over an unstable patch, and $a$ is defined empirically at 0.8–0.95 (Dillon 1982; Wijesekera et al. 1993). In the case of turbulence driven by hydraulic and convective processes at regions where flow encounters sloping topography, the Thorpe scale can overestimate the Ozmidov scale (Mater et al. 2015). Each overturn is delimited from the zero crossings of the depth-integrated Thorpe displacements starting from the surface to the seafloor. Thorpe displacements are computed on potential temperature instead of density to remove the noise associated with salinity spikes; as the temperature–salinity ($T$–$S$) properties in the canyon are very nearly linearly related, this choice does not bias the results. A minimum overturn height of 5 m is chosen from the overturn resolution (Galbraith and Kelley 1996). A temperature noise level of 0.001°C is defined from the standard deviation of detrended profiles within homogeneous layers. To remove the effect of random noise on the detection of overturns in weakly stratified waters, intermediate profiles with temperature increments larger than the noise level are first constructed (Ferron et al. 1998; Gargett and Garner 2008) before determining Thorpe displacements.

An alternative indirect estimate for the turbulence levels is derived from finescale observations of vertical kinetic energy (VKE) estimated from the LADCP vertical velocity profiles (Thurnherr et al. 2015). We use version 1.2 of the public implementation available online (at http://www.ldeo.columbia.edu/LADCP). The resulting profiles of $\varepsilon_{VKE}$ provide estimates for turbulent dissipation for the stations where no microstructure data were collected. Vertical wavelengths between 100 and 640 m were used to fit the VKE spectra. A comparison between $\varepsilon_{VKE}$ and the corresponding microstructure-derived values in the joint DMP/CTD profiles indicates agreement within a factor of 2 (appendix B), consistent with previous data (Thurnherr et al. 2015).

For each DMP/CTD profile, the kinetic energy $[E_{KE} = 0.5\rho(\langle u^2\rangle + \langle v^2\rangle)]$ and the available potential energy ($E_{PE} = 0.5\rho\overline{N^2}\langle\zeta'^2\rangle$), both depth integrated, are inferred from integrated (100–256-m wavelengths) vertical wavenumber spectra (denoted by $\langle\cdot\rangle$) in 512-m-thick, half-overlapping segments of horizontal velocities and isopycnal displacement. Isopycnal displacements $\zeta(z, t)$ are estimated (Clément et al. 2014) from the difference between each density profile $z(\gamma_n, t)$ and from a background density $z_{ref}(\gamma_n)$ chosen west and east of the sill. The neutral density surface $\gamma_n$ is the closest approximation to the surface along which a water parcel spread without experiencing buoyancy force (Jackett and McDougall 1997).

The ratio of the counterclockwise (CCW) to clockwise (CW) shear variance with depth for each MMP informs about the vertical direction of internal wave energy propagation (Waterman et al. 2013). A dominant counterclockwise (clockwise) component indicates downward-propagating (upward propagating) energy (Leaman and Sanford 1975). The shear-to-strain ratio $R_\omega = \langle V_z^2\rangle/(\overline{N}\langle\zeta_z^2\rangle)$, equivalent to the ratio of horizontal kinetic energy to potential energy, provides information on the internal waves' frequency content (Kunze et al. 1990a;

Polzin et al. 1995). Near-inertial waves, which are characterized by an intensified shear, have a large $R_\omega$, whereas a lower strain and reduced $R_\omega$ characterize higher-frequency waves (Kunze et al. 1990b). The strain $\langle \zeta_z^2 \rangle$ and shear variance $\langle V_z^2 \rangle$ as well as the rotary components of the shear variance (CCW and CW) are estimated using integrated vertical wavenumber spectra between 70 and 256 m. A Hanning window is applied on each detrended 256-m segment with 50% overlap. The shear is obtained by first differencing horizontal velocities. The strain $[(N^2 - \overline{N}^2)/\overline{N}^2]$ is calculated from the buoyancy frequency $N$ using the change in stratification relative to a reference stratification $\overline{N}$, which is defined from a running mean on three half-inertial periods of the 50-m low-pass stratification. Patterns of shear-to-strain ratios at MMP P1 and P3 are not significantly affected by using a running mean on one or five half-inertial periods.

## 3. Results

### a. *Time-averaged hydrography and flow in the canyon*

Moorings P1 and P3 sampled an along-canyon, 2-layer mean flow composed of an up-canyon deep transport below an opposing flow (Fig. 3). Because of instrument configuration errors, sampling of the P1 MMP did not reach the maximal eastward velocity; the two interpolations displayed in Fig. 3b show different spline interpolations corresponding to the strongest and to mean zonal velocity profiles. The inferred vertical shear of the mean profile below the zonal velocity maximum is significantly greater for the interpolation at P1 than at P3. The mean sampled velocities in both layers were larger at P1 than at P3; the corresponding lower-layer velocities below ≈3900 m are 5.2 ± 2.0 and 1.8 ± 0.4 cm s$^{-1}$. The velocity standard errors (pink lines in Figs. 3b and 3d) were calculated using the integral time scales (12 days, depth-averaged at MMP P1) of the 2-day low-pass filtered velocities to estimate the number of degrees of freedom (29, depth-averaged at MMP P1). The mean lower-layer velocity is indistinguishable from the average eastward velocity of 1.6 ± 1.3 cm s$^{-1}$ in the bottommost 300 m recorded during a 2-yr deployment in the 1990s in a deep depression of the BBTRE canyon near 17.80°W (Thurnherr et al. 2005). [The data from the BBTRE mooring, which did not measure the top 500 m of the canyon below its rims, do not show any indication of the westward flow in the shallower layer.] Strong tides superimposed on the mean flow cannot regularly reverse the lower-layer flow below ≈4100 m (dashed pink lines in Fig. 3b). A cross-canyon hydrographic section at the overflow (contours in Fig. 3a) as well as near-bottom LADCP measurements (not shown) suggest that the lower-layer eastward flow at the overflow section extended across the canyon width. Based on the moored data (Figs. 3b,d), eastward flow in the lower layer is strongest near the thalweg, along the steeper and less corrugated southern canyon wall. The available hydrographic and LADCP data from the downstream section indicate a similar situation there (not shown). At P1, the westward mean flow of the upper layer extended above the canyon rims, at least up to the shallowest current meter (−0.8 ± 0.3 cm s$^{-1}$ mean zonal velocity at 3200 m), whereas no significant zonal flow was observed above the canyon rims at P3.

The time-averaged separation between the two layers, based on the zero crossings of the mean zonal MMP velocities, occurs on the same neutral density surface ($\gamma_n = 28.13$) at both mooring sites. Because of the mean along-canyon density gradient between the two mooring sites, the interface is ≈50-m shallower (3870 m) in the overflow section at P1 than farther downstream at P3 (3920 m; Fig. 3). At P1, the mean density stratification in the lower layer is considerably higher than the corresponding stratification in the upper layer (Fig. 4b).

Along-canyon isopycnals $\gamma_n$ along the thalweg (stars in Fig. 1b) reveal the presence of a unidirectional along-canyon density gradient below ≈3500 m, with the largest gradient coinciding with the overflow (Fig. 2a). The cross-sill density drop there corresponds to a 0.2°C warming of AABW at P1 over less than 5-km along-canyon distance, about twice the magnitude of the entire warming between the overflow and the downstream moorings (≈100 km of canyon). The density drop in the overflow region implies markedly different stratifications east and west of the sill. The corresponding mean of CTD profiles (Fig. 4b) shows a pronounced buoyancy frequency maximum, with a peak value of $1.2 \times 10^{-3}$ s$^{-1}$ between 3800 and 4000 m, west of the overflow sill and noticed as far as 15.3°W. East of the sill no similar buoyancy frequency maximum was observed; the buoyancy frequency in the corresponding mean profile ranges around $10^{-3}$ s$^{-1}$.

In the BBTRE data, a significant correlation between intensified along-canyon density gradients and high topographic peaks between station pairs persists across more than 1000 km of the canyon (Thurnherr et al. 2005). The red and black line segments along the bottom of Fig. 2a show the along-thalweg density gradients and their uncertainties, respectively. For station pairs where the blocking depth of abyssal hills is shallower than the shallower of the two bracketing profiles, the density is averaged in the 50 m above the blocking depth. Based on five yo-yo stations with six to eight profiles in the canyon (Fig. 1), the high-frequency density uncertainty, primarily of tidal and near-inertial origin, remains below

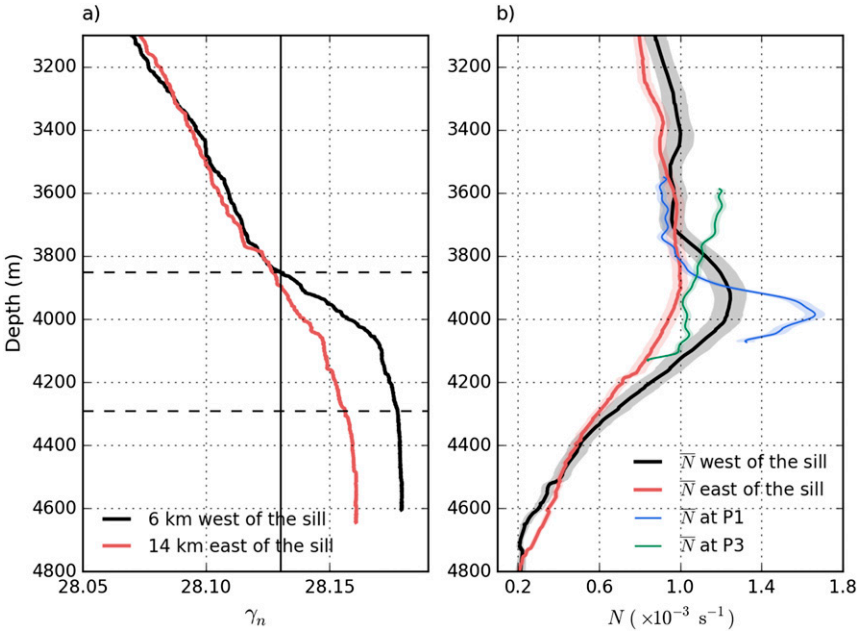


FIG. 4. (a) Individual CTD density profiles taken west (black) and east (red) of the sill. The shallowest depth at the narrow deep passage over the sill 4290 m and the bifurcation depth at 3850 m are indicated (dashed lines); the vertical line indicates the 2-layer interface at 28.13. (b) Averaged buoyancy frequency and its standard error (shaded region) from CTD profiles west (black) and east (red) of the sill and at the mooring P1 (blue) and P3 (green).

$4 \times 10^{-3}\,\mathrm{kg\,m^{-3}}$, consistent with previous measurements in this region (Thurnherr and Speer 2003). At the spatial resolution of the along-canyon measurements (≈15-km average station spacing between 14° and 15°W in Fig. 2), the only density gradient rising above the high-frequency noise occurs in the overflow where the along-canyon density gradient reaches $1.6 \times 10^{-6}\,\mathrm{kg\,m^{-4}}$. Downstream of the overflow, the amplitude of the along-canyon density gradient in the near-bottom water remains below $2.9 \times 10^{-7}\,\mathrm{kg\,m^{-4}}$, which is indistinguishable from its uncertainty.

To estimate up-canyon volume transport, the time-averaged zonal velocity at P1 and P3 (Fig. 3) is integrated across the entire canyon width of $1.9 \times 10^{6}$ and $2.6 \times 10^{6}\,\mathrm{m^2}$, respectively. The velocities along the thalweg are assumed representative in the across-canyon direction; frictional boundary layers along the sidewalls, in particular, are ignored. To estimate the velocity between the MMP profiles and the deep current meters, we apply a fourth- and seventh-order polynomial fit (Fig. 3) at P1 and P3, respectively. The resulting up-canyon transport of the deep layer in the overflow and downstream regions are 0.10 ± 0.03 and 0.04 ± 0.01 Sv ($1\,\mathrm{Sv} = 10^{6}\,\mathrm{m^3\,s^{-1}}$), respectively. While this layer is mostly enclosed by the canyon sidewalls in the two mooring regions, there are deep passages cross cutting the canyon walls between the mooring arrays (Fig. 1). The inherent uncertainty arising from possible intercanyon exchange through these passages as well as diapycnal upwelling may contribute to the transport difference at the mooring sites.

Velocity spectra of Nortek current meter data are integrated over several different frequency ranges (Fig. 5) to quantify the kinetic energy of the subinertial flow ($<0.8f$, with an inertial period of 33.4 h), of semidiurnal tides ($0.8M_2$–$1.2M_2$), of near-inertial waves ($0.8f$–$1.2f$), and of high-frequency waves ($1.2M_2$–$N$). As expected, the subinertial kinetic energy (KE) is highest in the overflow (P1). In the narrow passage of the sill, the subinertial KE is $35.0\,\mathrm{cm^2\,s^{-2}}$ ~10 m above the seabed (P1a); 770 m above the seabed at 3500 m (P1b), the subinertial KE is $16.9\,\mathrm{cm^2\,s^{-2}}$. In the deep instrument over the sill (P2a), the subinertial KE is $14.1\,\mathrm{cm^2\,s^{-2}}$; in the other instrument records, the subinertial KE remains below $10\,\mathrm{cm^2\,s^{-2}}$.

In contrast to the subinertial flow, semidiurnal KE is highest in the bottom instrument of every mooring, with particularly high values in the overflow region (P1a and P2a). These observations indicate the presence of significant baroclinic tides in the canyon with amplitudes that increase with depth. Compared to P3 and P4, the internal tide is amplified both at P1 and P2, with the greatest amplification outside the deep overflow passage at P2a. Inside the narrow sill passage (at P1a), the semidiurnal and

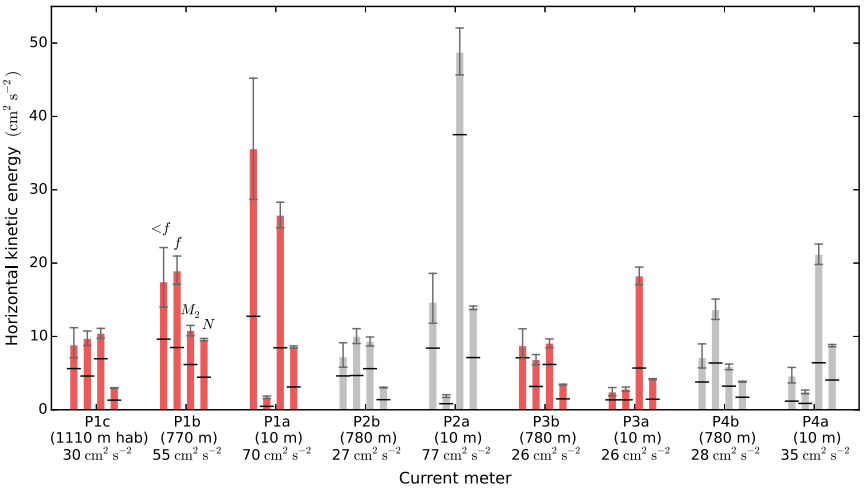


FIG. 5. Horizontal kinetic energy of the subinertial flow ($<0.8f$) of near-inertial waves ($0.8f$–$1.2f$) of semidiurnal tides ($0.8M_2$–$1.2M_2$) and of high-frequency waves ($1.2M_2$–$N$) for each Nortek current meter at moorings P1, P2, P3, and P4 (Fig. 3). P1a and P1b correspond to the current meters at 10 and 770 m (hab), respectively. The 95% confidence intervals, band averaged for each frequency range, are inferred from the equivalent degree of freedom of 50% overlapping segments after applying a Hanning window. The total horizontal kinetic energy summed over the four frequency ranges is indicated below each instrument. The black line separates the contribution of zonal (below) and meridional (above) velocities.

subinertial KE are of similar magnitudes and dominate the total energy. In the current meters on the same mooring but higher up in the water column, the subinertial flow contributes less and near-inertial oscillations contribute more to the total energy, which increases by a factor of 2 from the shallowest (P1c) to deepest (P1a) current meter.

In contrast to the subinertial and semidiurnal KE, both of which are strongest deep in the canyon, enhanced near-inertial KE is confined to the shallower current meters near the depth of the canyon rims at each site. At 10 m above the seafloor, the near-inertial energy is reduced in every record. The largest near-inertial peak was observed at 3500 m above the narrow sill passage (P1b) in the core of the upper-layer return flow near the depth of the canyon rims. With 18.4 cm$^2$ s$^{-2}$, near-inertial oscillations contribute to 29% of the total variance, whereas their contribution in the bottom layer (P1a) is only 2% (1.2 cm$^2$ s$^{-2}$). Above P1b, the near-inertial KE reduces upward, as illustrated by the P1c record collected ≈300 m higher up in the water column at 3200 m, where the near-inertial KE is 9.2 cm$^2$ s$^{-2}$. Downward decrease of near-inertial KE inside the BBTRE canyon was previously noted at a different site (Toole 2007) and potentially attributed to lateral constriction by the canyon walls and to the presence of a vertically variable shear and stratification.

### b. *Turbulent mixing inside the canyon*

The along-canyon finestructure dissipation $\varepsilon_{\mathrm{VKE}}$, depth averaged in the deepest 1000 m (Fig. 2b), reveals mean turbulence levels ranging from $O(10^{-10})$ W kg$^{-1}$ downstream from the overflow during neap tides to about $4 \times 10^{-9}$ W kg$^{-1}$ in the overflow during spring tides. Between the two mooring arrays, the observed averages are around $5 \times 10^{-10}$ W kg$^{-1}$. This pattern emphasizes the role of the sill in the deep-water modification, suggested by the large cross-sill density gradient around P1. At both mooring sites, the fortnightly tidal cycle modulates $\varepsilon_{\mathrm{VKE}}$ (by an order of magnitude in the overflow region and about a factor of 5 at P3). The reversed fortnightly modulation of $\varepsilon_{\mathrm{VKE}}$ near 14.5°W is likely an artifact of spatial variability, as more neap tide than spring tide measurements were collected over the corrugated northern canyon wall.

While LADCP-derived $\varepsilon_{\mathrm{VKE}}$ informs on the temporal and horizontal distribution of turbulence in the canyon, they are indirectly derived from energy estimates of the internal wave field. More direct and much higher vertical resolution estimates of turbulent dissipation are available from the microstructure survey (Fig. 1). Spring- and neap-averaged microstructure profiles were calculated for the overflow region and for the remainder of the canyon (Fig. 6). Profiles from the overflow region include the midcanyon cross sill and the northern wall transects (Fig. 1). In the overflow region below 3500 m (Fig. 6b), the averaged $\varepsilon$ is one order of magnitude higher, $1.8 \times 10^{-9}$ W kg$^{-1}$ (95% confidence interval of 0.6–3.5 $\times 10^{-9}$ W kg$^{-1}$), during spring compared to neap tides, $1.2 \times 10^{-10}$ W kg$^{-1}$ (0.6–2.3 $\times 10^{-10}$ W kg$^{-1}$),

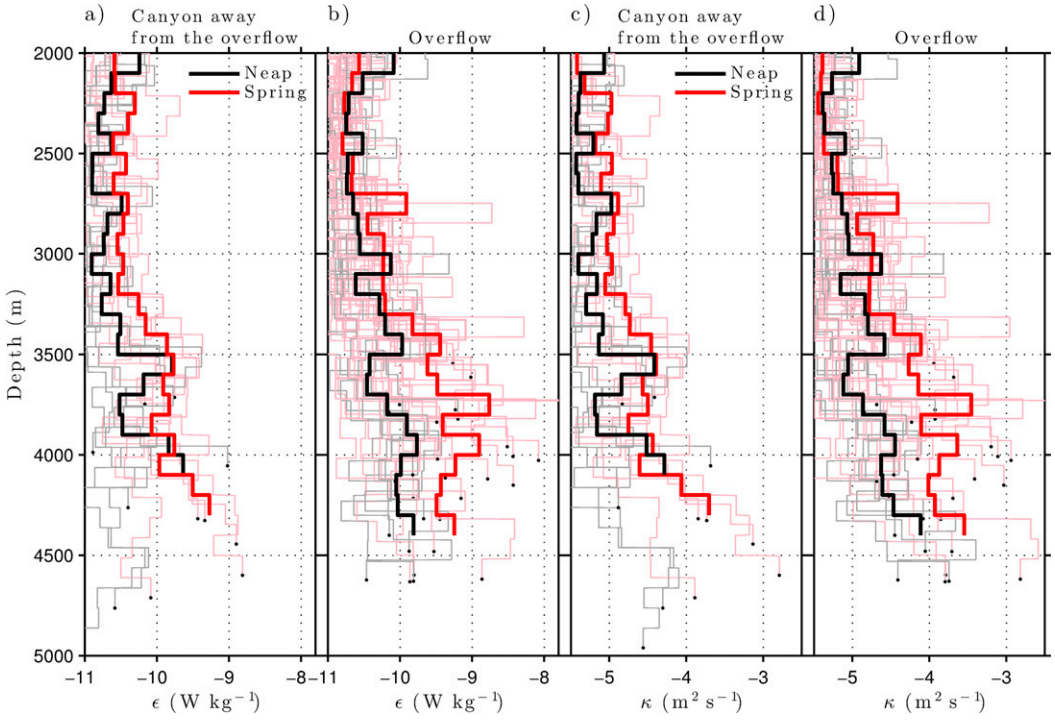


FIG. 6. Dissipation rate of turbulent kinetic energy $\varepsilon$ from microstructure profilers (gray and light red for neap and spring tides, respectively) measured inside the canyon (a) away from the sill and (b) around the sill at the overflow site; $\varepsilon$ is averaged for the spring (red) and neap (black) tides. (c),(d) As in (a) and (b), but for the diapycnal diffusivity $\kappa$. The terms $\varepsilon$ and $\kappa$ are averaged in potential temperature space before being converted back to depth space.

and also compared to the rest of the canyon, $1.7 \times 10^{-10}\,\mathrm{W\,kg^{-1}}$ ($1.0$–$2.6 \times 10^{-10}\,\mathrm{W\,kg^{-1}}$). This depth range of enhanced $\varepsilon$ encompasses the 2-layer interface as well as the stratification maximum in the overflow. In the microstructure profiles, the neap tide dissipation rates in the overflow region are not significantly higher than the neap tide dissipation rates in the remainder of the canyon (Figs. 6a,b). Using Osborn's model (Osborn 1980), $\kappa = N^{-2}\Gamma\varepsilon$ with a constant mixing efficiency ($\Gamma = 0.2$), we infer the diapycnal diffusivity $\kappa$ (Fig. 6) from $\varepsilon$. The spring–neap cycle modulates $\kappa$ below 3500 m at the sill, with a depth-averaged $\kappa$ ranging between $3.8 \times 10^{-4}$ (spring tides; 95% confidence interval of $1.4$–$7.5 \times 10^{-4}\,\mathrm{m^2\,s^{-1}}$) and $3.0 \times 10^{-5}\,\mathrm{m^2\,s^{-1}}$ (neap tides; $1.6$–$5.1 \times 10^{-5}\,\mathrm{m^2\,s^{-1}}$) with maxima of $3.8 \times 10^{-3}\,\mathrm{m^2\,s^{-1}}$.

Away from regions of internal wave generation, there is generally a close relationship between internal wave energy and turbulence (Gregg 1989; Polzin et al. 1995). Having observed a spatially varying dissipation rate enhanced at the sill, it becomes relevant to assess the relationship between an intensified $\varepsilon$ and the internal wave field. Integrated microstructure dissipation rates times the density $\int \rho\varepsilon\,dz$ over the bottommost 1000 m and above the canyon walls are compared in Fig. 7 to the sum of kinetic and potential energy of the internal wave field $E_{\mathrm{KE}} + E_{\mathrm{PE}}$. (The definition of $E_{\mathrm{KE}}$ and $E_{\mathrm{PE}}$ must be cautiously interpreted because the separation between the deep overflow and the internal wave field is blurred by their similar vertical scales and periods of variability.) Inside the canyon (Fig. 7a), the correlation coefficient between the integrated dissipation rate and $E_{\mathrm{KE}} + E_{\mathrm{PE}}$ is significant at 95% at the overflow site ($r = 0.36$, $p < 0.01$) but not outside the overflow region ($r = 0.44$, $p = 0.06$). Above the lateral canyon walls [1000–2000-m height above bottom (hab); Fig. 7b], the corresponding correlation is also significant above the overflow ($r = 0.53$, $p < 0.01$) but not elsewhere ($r = 0.38$, $p = 0.12$). Those correlations support the hypothesis of a driving of turbulent mixing by internal waves over the sill. Within the canyon at the sill region, in addition to the internal wave field, localized turbulence-generating processes characterized by large outliers around $0.5\,\mathrm{mW\,m^{-2}}$ (Fig. 7a) may not be accurately represented by $E_{\mathrm{KE}}$ and $E_{\mathrm{PE}}$.

### c. *Overflow region*

Further insight into the role of the sill is gained from four across-sill tow-yo sections and from microstructure

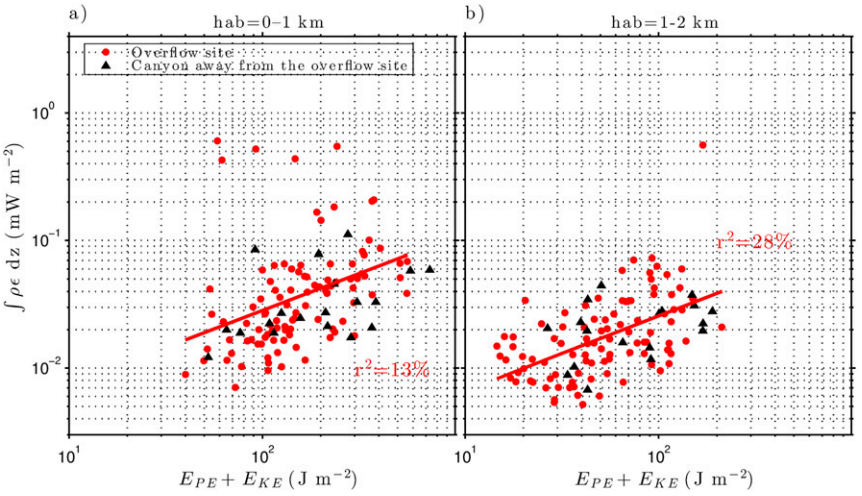


FIG. 7. Total energy of the internal wave field inferred from CTD/LADCP profiles in 640-m segments vs depth-integrated dissipation rate of turbulent kinetic energy measured by microstructure profilers. Measurements at the overflow site (red) and away from the overflow site in the canyon (black) were taken at (a) 0–1 and (b)1–2 km hab.

profiles taken at middistance from the canyon rims (Fig. 1). Only one out of the four tow-yos sampled during spring tides; Fig. 8 displays the spring tide and one of the neap tide transects. In both sections the ship transited from east to west and both were timed for eastward tidal flow to occur during passage of the sill. Those sections reveal an asymmetric cross-sill spring–neap modulation of isopycnal displacements and dissipation rates. During spring tides (Fig. 8a), the isopycnals around the 28.12–28.14 neutral surfaces are squeezed on the upstream side of the sill, plunge down over the sill crest, and then rebound downstream of the sill with $O(100)$ m vertical displacements, reminiscent of an internal hydraulic jump. The isopycnal displacements extending at least up to the 28.10 surface are perhaps related to a forming lee wave. The corresponding isopycnal surfaces are less disturbed during neap (Fig. 8b) than spring tides, independently of the semidiurnal tidal phase (clock symbols), as confirmed by the two additional neap tide sections. During spring tides, the stratification between the 28.12 and 28.14 neutral surfaces is increased both upstream and downstream of the sill, although the effect is much stronger upstream.

Elevated dissipation rates during spring tides, up to $1.8 \times 10^{-7}$ W kg$^{-1}$ in individual profiles (Fig. 8c), are found over the sill crest within 1.7 km east of the sill, that is, in the same region where the isopycnals show large vertical displacements. While there are clear spring–neap differences in flow and turbulence in this region, there is no apparent correlation between the semidiurnal tidal phase (clock symbols) and $\varepsilon$ in the four spring tide profiles. Even though it is based, in part, on a single profile collected ≈2.3 km west of the sill saddle, the observed pattern of turbulence across the sill is consistent with a unidirectional hydraulically controlled overflow, where high turbulence can arise from shear instabilities in the supercritical region downstream of the sill and from the transition between a supercritical to subcritical regime (hydraulic jumps). In the latter case, an exchange from kinetic to potential energy occurs in the lower layer as the isopycnal rebounds.

The cross-sill density gradient (Fig. 4a) and the mean flow acceleration at P1 provide additional support for the hypothesis that the overflow in the BBTRE canyon near 14.6°W is hydraulically controlled. Several lines of indirect evidence support the inference of internal hydraulic control. First, the observed mean transport at P1 is close to predictions from the inviscid 1.5-layer hydraulic model of Whitehead et al. (1974). In this steady-state model, the volume transport is inferred by applying Bernoulli's law to the active lower layer, in which the conservation of potential vorticity and the geostrophic balance apply. The predicted volume transport $Q$ depends on the Coriolis parameter $f$, the reduced gravity at the layer interface $g'$, the width of the sill passage $W$, as well as the upstream thickness of the lower-layer $h_u$. For overflows that are narrow compared to the baroclinic deformation radius,

$$Q = \frac{2^{3/2}}{3} W\sqrt{g'}\left(h_u - \frac{f^2W^2}{8g'}\right)^{3/2}. \qquad (1)$$

Applying this 1.5-layer model to the continuously stratified ocean requires estimates for $g'$ and $h_u$.

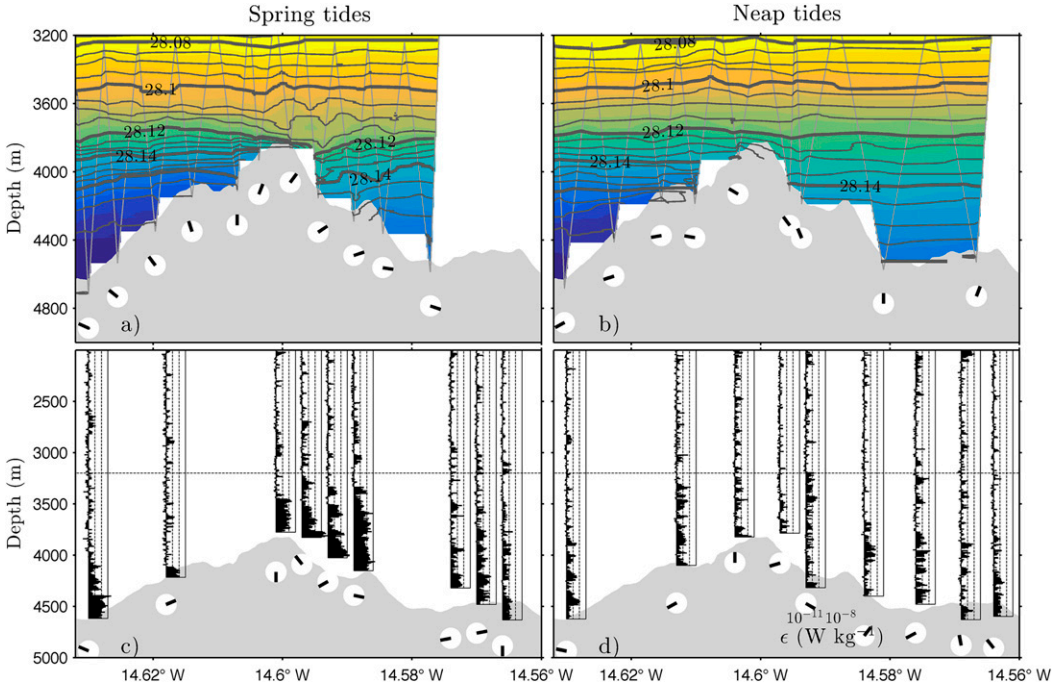


FIG. 8. (a),(b) Neutral density across the sill measured by two 8-h tow-yo sections during (left) spring and (right) neap tides. (c),(d) Dissipation rate $\varepsilon$ sampled by microstructure profilers around the sill during (left) spring and (right) neap tides. The term $\varepsilon$ is displayed in logarithmic scale from $10^{-11}$ to $10^{-8}$ W kg$^{-1}$. The time relative to the maximum eastward tidal flow referenced at 1200 UTC is indicated below each profile. The dashed line of the bottom subplots corresponds to the upper limit of the upper subplots.

Following Whitehead (1998), $g' = 2.0 \times 10^{-4}\,\mathrm{m\,s^{-2}}$ is estimated from the maximum upstream–downstream density difference ($\Delta\rho = 0.02$) above the sill depth in two profiles straddling the sill (orange stars in Fig. 1), and the thickness of the lower-layer $h_u = 440$ m is taken from the depth difference between the sill saddle and the so-called bifurcation depth, where upstream and downstream density profiles diverge (Fig. 4). The passage width $W = 2$ km, usually defined at the bifurcation depth, is approximated at P1 by the width of the narrow deep passage, which constrains most of the lower layer. The Rossby radius $L = (2g'h_u/f^2)^{1/2} = 10$ km, with $f = 5.2 \times 10^{-5}\,\mathrm{s^{-1}}$, confirms that the overflow passage is narrow. With these parameters expression 1 yields a transport estimate of 0.14 Sv in good agreement with the observed mean transport at P1, especially considering the model's simplifying assumptions that include no friction and mixing as well as a rectangular channel geometry (Whitehead 1998).

One of the defining characteristics of hydraulic control is that the flow speed at the control point (a sill or narrows) is equal to the horizontal speed of gravity waves, in which case the flow is called critical. Using the parameters given above, the corresponding 1.5-layer gravity wave speed $c = \sqrt{g'h_u} = 30\,\mathrm{cm\,s^{-1}}$ is close to the velocity maximum in the deep layer of 25 cm s$^{-1}$ at P1, consistent with the inference of hydraulic control. One final piece of evidence for hydraulic control is provided by the observation of a significant correlation ($r = -0.78$, $p > 0.01$) at P1 between potential temperature and zonal velocity, both depth-averaged below 3900 m. Given the small horizontal density gradients in the canyon upstream of the overflow, the cold, dense water advected across the sill must be uplifted from greater depths. Uplift of deep upstream water is termed Bernoulli aspiration (Kinder and Bryden 1990) and is commonly observed in hydraulically controlled overflows, where it is attributed to a reduction in dynamic pressure by the accelerating flow at the sill.

To determine whether this uplift is sufficient to transport the deepest upstream water across the sill, we derive an order of magnitude estimate for the blocking depth $U/N$ at P1. Using $N = 10^{-3}\,\mathrm{s^{-1}}$, the blocking depth during maximum eastward tidal flow ($u \approx 25\,\mathrm{cm\,s^{-1}}$) is 250 m, similar in magnitude to the elevation of the sill above the upstream basin (≈400 m at the thalweg); we infer that there is no significant topographic blocking of eastward-flowing deep canyon water in the overflow. During maximum westward tidal flow ($u \approx -5\,\mathrm{cm\,s^{-1}}$), on the other hand, the blocking-depth estimate is only

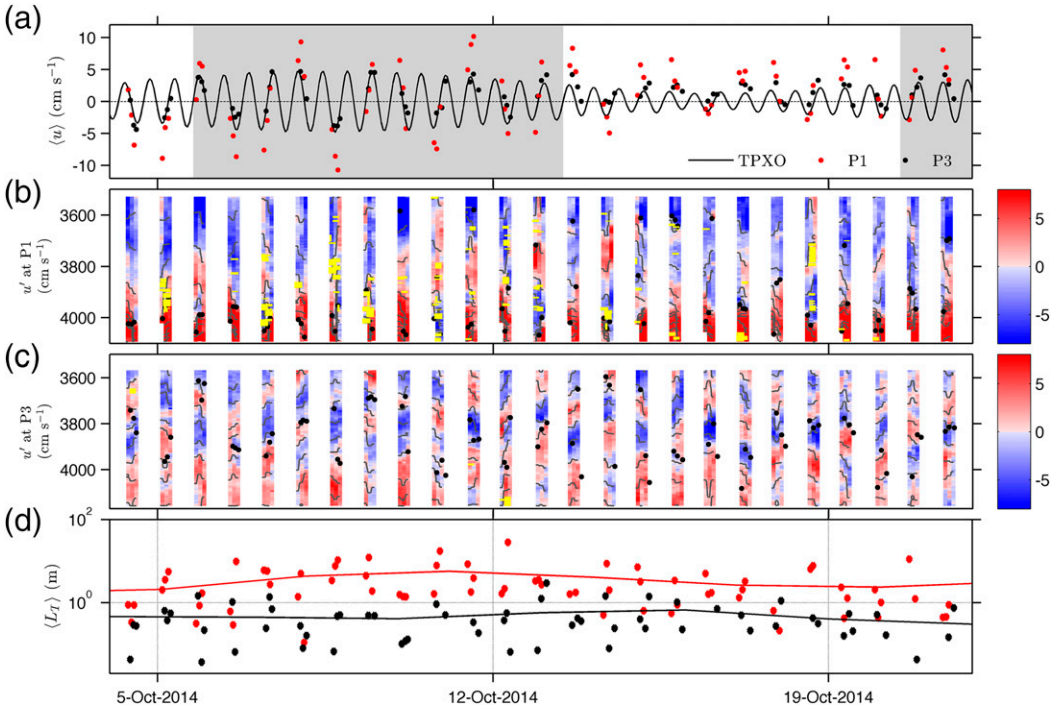


FIG. 9. (a) Depth-averaged zonal velocity at MMP P1 (red dots), at MMP P3 (black dots), and from TPXO (black line, for the eight components $M_2$, $S_2$, $N_2$, $K_2$, $K_1$, $O_1$, $P_1$, and $Q_1$); the gray shading indicates the spring tides. Zonal velocity (colors) minus the depth-averaged velocity, isopycnals (black lines), depth of maximum shear (black dots), and occurrence of temperature overturns (yellow) at (b) P1 and (c) P3. (d) Depth-integrated Thorpe scales at P1 (red dots) and P3 (black dots) with the 7-day low-pass filtered values (lines).

50 m, that is, tidal reversals of the overflow affect only the top of the lower layer. The lower-layer water downstream of the overflow is topographically constricted to flow unidirectionally up canyon, independently of the tidal phase.

### *d. Tidal modulation of turbulence*

Using data from the two MMPs, P1 at the overflow site and P3 at the downstream site, we investigate the tidal modulation of turbulent patches in the canyon with a Thorpe-scale analysis (Fig. 9). Elevated depth-averaged Thorpe scales $\langle L_T \rangle$, assuming zero turbulence where no overturns are observed ($L_T = 0$), occur in the overflow with a mean and standard error of $2.8 \pm 0.1$ m, compared to $0.9 \pm 0.02$ m at P3. Overturns are observed in 20% of the measurements at P1 as opposed to 5% at P3. The largest $\langle L_T \rangle$ occurs at P1 with 28% values larger than 10 m compared with 19% at P3. The observed maximum height of static instability was 200 m at P1. In addition to the intensified mean $\langle L_T \rangle$ at P1, spring–neap tides modulate $\langle L_T \rangle$ by a factor of 2–3, whereas Thorpe scales at P3 are not significantly modulated on this time scale. Despite the presence of fortnightly modulated overturns and microstructure $\varepsilon$, a comparable periodicity in the lower-layer subinertial eastward flow potentially arising from the buoyancy forcing of the downstream enhanced turbulence (St. Laurent et al. 2001a) could not be ascertained.

Along with the fortnightly modulation of Thorpe scales, we investigate the presence of a semidiurnal cycle in the occurrence of large overturns at P1. A composite analysis based on semidiurnal tidal phase, taken from the hourly TPXO tidal prediction, reveals elevated $\langle L_T \rangle$, by up to factors of 2 and 4 during neap and spring tides, respectively, occurring during westward tidal flow (Fig. 10). During this semidiurnal tidal phase, the maximal westward tidal flow reverses the mean up-canyon flow almost to its deepest measurement at MMP P1 around 4100 m, as seen from the 10th percentiles of velocities (Fig. 3b). During times of westward tidal flow, advection of warmer (downstream) water reduces the stratification in the overflow (Fig. 11c). Many of the largest overturns were observed in all three consecutive profiles collected during every MMP sampling burst, implying decay time scales greater than 3 h, consistent with the period of increased $\langle L_T \rangle$ composite.

During eastward tidal flow, $\overline{L_T}$ does not vary significantly over the fortnightly cycle, with the mean Thorpe scales at P1 increasing from ≈1 m at 3600 m to 4 m near the seabed (Fig. 11b). During westward tidal flow,

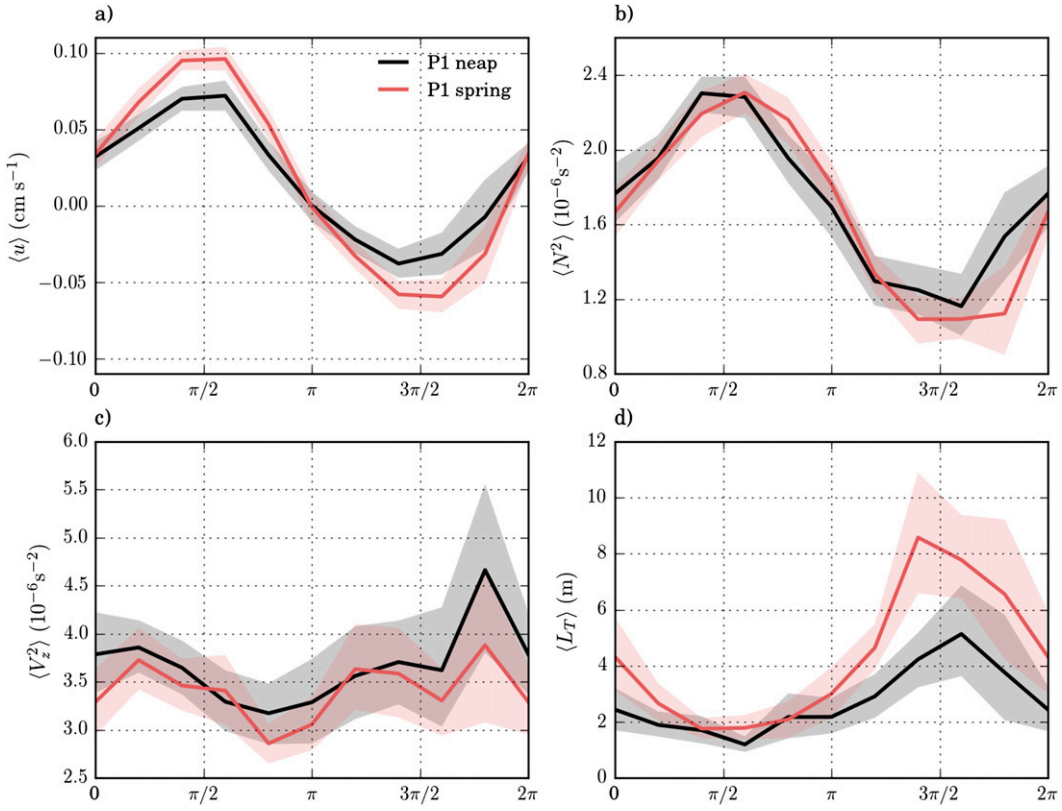


FIG. 10. (a) Zonal velocity, (b) buoyancy frequency squared, (c) shear variance, and (d) Thorpe scales depth-averaged from 3800 to 4000 m at varying semidiurnal phase (0 and $3\pi/2$ correspond to southward and westward tidal flow, respectively) for spring (red) and neap (black) tides at MMP P1.

$\overline{L_T}$ is elevated between 3600 and 4000 m, with a local maximum near 3850 m; at neap tides, tidal modulation is about a factor of 2, whereas the corresponding factor for spring tides is 3–4. The vertical structure of $\overline{L_T}$, including its middepth maximum, agrees well with the vertical structure of microstructure-derived $\varepsilon$ in the overflow (Fig. 6b).

The microstructure observations from the lee of the overflow sill (Fig. 8c) suggest that hydraulic jumps contribute to the overall turbulence, including to its vertical structure with its middepth maximum, in the overflow region. The apparent absence of semidiurnal modulation in microstructure observations (Fig. 8c) implies that other processes than hydraulic jumps must affect $\overline{L_T}$. Next, we consider shear instabilities associated with the overflow as well as with the internal wave field as possible alternative explanations for the $\overline{L_T}$ middepth peak. The ratio of stabilizing density stratification to destabilizing vertical shear, quantified in the gradient Richardson number ($\mathrm{Ri} = N^2/V_z^2$), allows evaluation of the necessary condition for shear instability $\mathrm{Ri} < 0.25$ (Miles and Howard 1964); in the following, $\mathrm{Ri}_c$ denotes the fraction of measurements below criticality. The Ri is calculated at large vertical resolution, using 10-m running-mean velocities and densities to filter out small-scale variability turbulent overturns. [The instabilities in the overflow region are caused by the combination of the tidally modulated overflow and the internal wave field. In addition to linear superposition, the two processes interact nonlinearly through critical layer absorption of internal waves (Koop and McGee 1986). Because of the common vertical and temporal scales of each process, no unambiguous separation of the two processes is applied.] A composite analysis in semidiurnal phase space of $\langle N^2 \rangle$ and $\langle V_z^2 \rangle$, depth-integrated around the 2-layer interface, confirms the predominant role of stratification (Figs. 10b,c). A $\langle N^2 \rangle$ reduction by 49% starts half a semidiurnal period before the $\langle L_T \rangle$ maximum. In addition to possible hydraulic control affecting the dissipation rate, the reduced $\langle N^2 \rangle$ associated with the deep sheared jet favors the onset of shear instability at the overflow site, with $\overline{\mathrm{Ri}_c}$ of 35% (averaged between 3800 and 4000 m in Fig. 11e) during westward tidal flow, as opposed to 23% during eastward tidal flow, but without affecting the fortnightly modulation of $\langle L_T \rangle$.

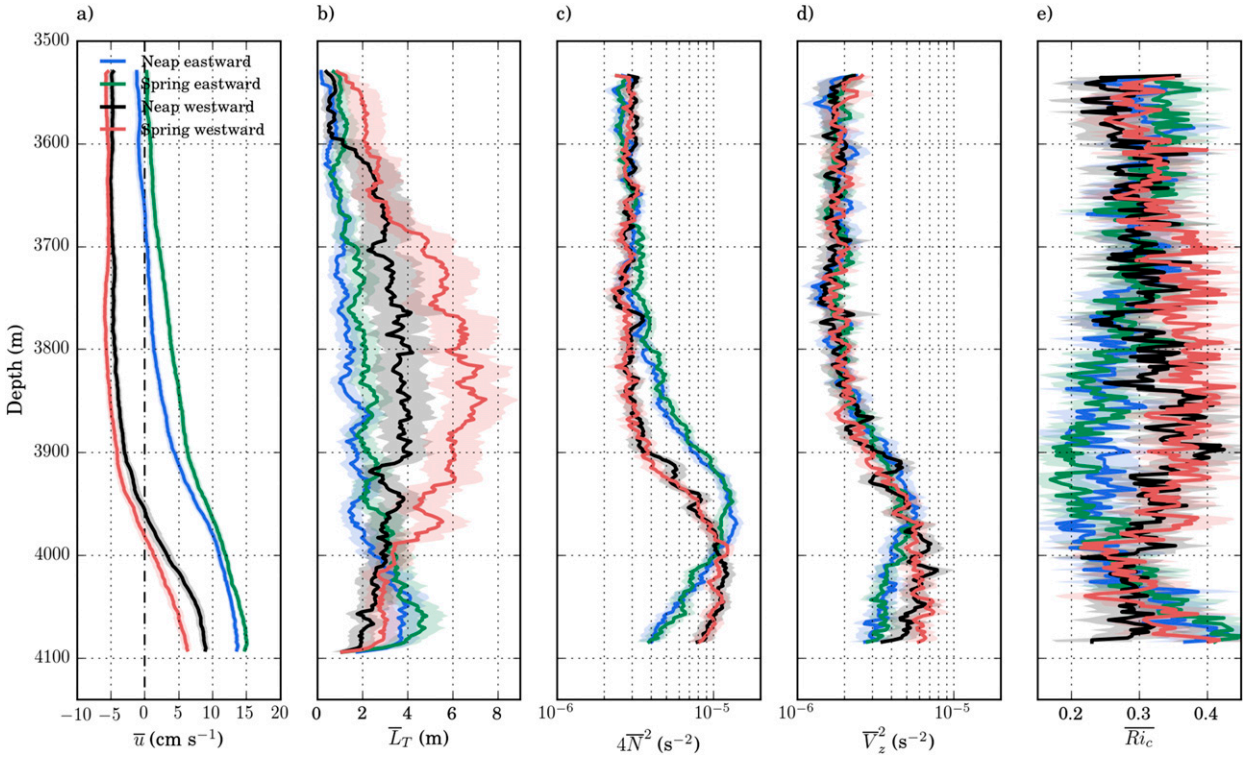


FIG. 11. (a) Zonal velocity, (b) Thorpe scales, (c) buoyancy frequency, (d) shear, and (e) fraction of Richardson number below criticality averaged for a semidiurnal eastward and westward tidal flow at spring and neap tides at MMP P1. Shading represents 95% confidence intervals inferred by bootstrapping.

### *e. Internal wave properties*

The internal wave field in the overflow and downstream regions (P1 and P3, respectively) is analyzed using the counterclockwise-to-clockwise polarization ratio of shear variance and the shear-to-strain variance ratio $R_\omega$. The polarization ratio at P3 (Fig. 12a) is dominated by the counterclockwise component throughout the entire profile and decreases with increasing depth. The internal wave field in this region away from the overflow is therefore predominantly associated with downward-propagating energy. The large shear-to-strain ratio at P3 (Fig. 12b), which is also associated with a decrease with increasing depth, indicates dominance of near-inertial waves outside the overflow. The downward-decreasing importance of near-inertial waves apparent in the finestructure properties is consistent with the vertical decrease in near-inertial energy inside the canyon (Fig. 5) and with possible trapping (Gordon and Marshall 1976; Hotchkiss and Wunsch 1982) and/or with lateral constriction of near-inertial waves in the canyon (Fig. 3). The importance of near-inertial waves away from the overflow agrees with elevated near-inertial finescale shear found at another site away from any overflow in the BBTRE canyon (Toole 2007).

In contrast to P3, the polarization ratios at P1 are close to zero, indicating that there is no preferred vertical propagation direction for the internal wave energy in the overflow. The corresponding shear-to-strain ratios in the overflow above 3900 m are close to 5, that is, 2–3 times lower than $R_\omega$ at P3, indicating lesser dominance of near-inertial waves and a stronger influence of high-frequency waves in the overflow region. Both the negative CCW/CW polarization and the lower $R_\omega$ in the shallowest sample at P1 during spring tides, compared to neap tides, suggest the presence of internal tides in the overflow at P1. In that case a lower shear-to-strain ratio is expected, and the dominance of a single wave to relate $R_\omega$ to the frequency content of the internal wave band may no longer be valid. To separate the semidiurnal tide from the remainder of the variability, least squares harmonic analysis (Thomson and Emery 2014) with the $M_2$ and $S_2$ tidal frequencies is used. Rotary spectra of the resulting semidiurnal shear (Figs. 12c,d) indicate the prevalence of the clockwise component with the upward-propagating energy characteristic of internal tides at vertical wavelengths above 90 m at P1. On

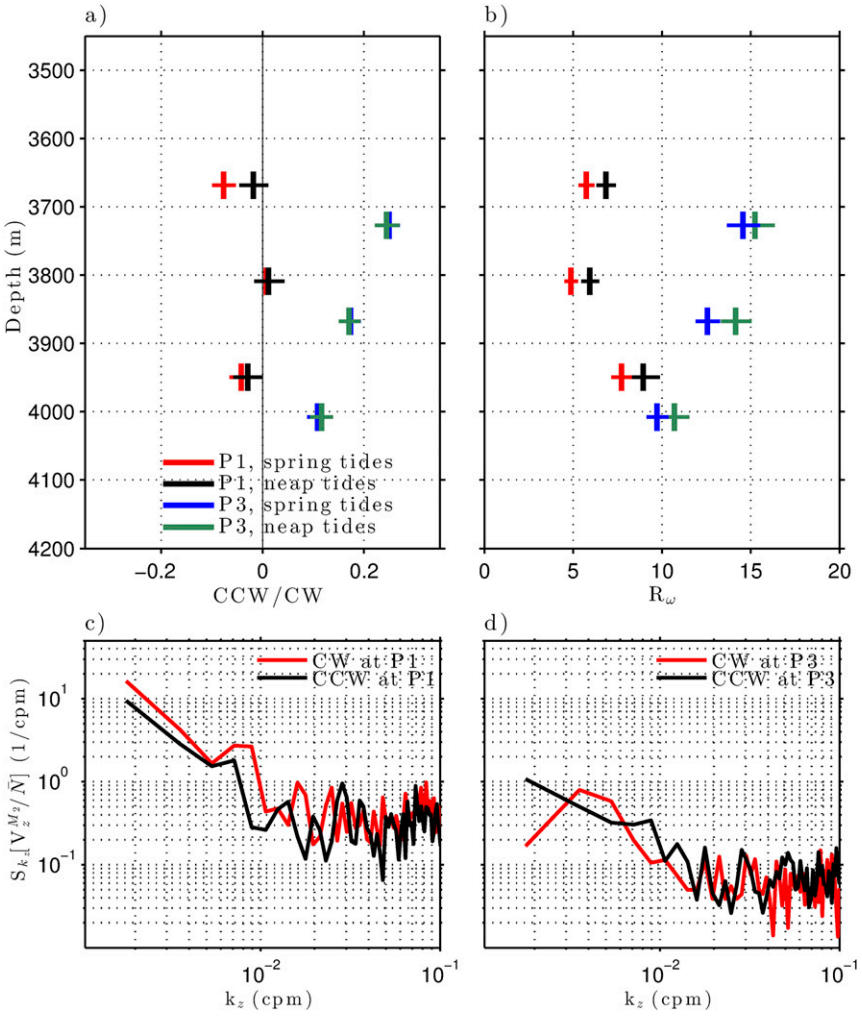


FIG. 12. (a) Ratio of the counterclockwise to clockwise component of the shear variance at MMP P1 and MMP P3 averaged for spring and neap tides; a positive ratio indicates downward-propagating energy of internal waves. (b) Shear-to-strain ratio $R_\omega$ at P1 and P3 averaged for spring and neap tides; near-inertial waves are characterized by a large $R_\omega$. In (a) and (b), the 95% confidence intervals (horizontal bars) are indicated based on bootstrapping. Clockwise (red) and counterclockwise (black) spectra of the shear filtered at $M_2$ and $S_2$ frequencies at (c) P1 and (d) P3.

these wavelengths, the semidiurnal shear spectra are red everywhere but characterized by higher energy at P1 versus P3.

## 4. Discussion: Energy of the overflow region

In the overflow region below ≈3800 m, the isopycnal surfaces are deeper east than west of the sill (Fig. 8), with the implied decrease of lower-layer potential energy across the sill accelerating the flow. Both interfacial shear instabilities and boundary friction near the seabed extract kinetic energy from the overflow. Internal waves (internal tides and quasi-steady lee waves) arise from flow–topography interactions (St. Laurent and Garrett 2002) and are likely generated at hydraulic jumps downstream of the overflow sill. These locally generated internal waves redistribute some kinetic energy by radiating energy out of the sill region. A local mechanism of energy loss at the hydraulic jump is accounted for by the drop in Bernoulli function $B = (1/2)\mathbf{u}^2 + gz + P/\rho$ across the sill, with $P$ and $z$ the pressure and the distance from the bottom, respectively.

The energy equation (Baines 1995) can be applied to the barotropic tides or to the overflow at the sill $\partial_t(E_{\mathrm{KE}} + E_{\mathrm{PE}}) = -\nabla \cdot (\rho \mathbf{u} B) + \rho \mathbf{u} \cdot \mathbf{F}$. The last two terms denote the energy flux and the frictional or turbulent

stresses **F**, respectively. The local energy sources and sinks, for example, via an energy conversion between barotropic tides and the overflow, are not accounted for. Such a conversion is partially represented by breaking internal waves, which can redistribute some energy of the barotropic tides and as such potentially affect the overflow, despite the absence of fortnightly modulation in the subinertial circulation. Over different shallower sills, the local energy dissipation within the interior and at the bottom boundary can compare with the Bernoulli drop (Nash and Moum 2001) and, along with the internal wave energy radiated, can significantly (Arneborg and Liljebladh 2009; Staalstrøm et al. 2015) or moderately (Klymak and Gregg 2004) contribute to the energy loss of barotropic tide. Despite the unknown barotropic energy loss within the fracture zone in deep water, we establish both the energy loss at the sill (with a focus on the lower layer) and the energy radiated by internal tides. This quantification informs about the potential location of energy dissipation. A comparison of the dissipation rate with the energy loss around the sill allows us to assess the role of the local hydraulic jump to the drop in the Bernoulli function.

### *a. Energy loss across the sill*

In a steady-state flow, the energy flux is first compared with the measured energy dissipation integrated in the volume $V$ of oriented surface $S$ around the sill, $\oint_S \rho B\mathbf{u}\cdot d\mathbf{S}$ versus $\int_V \rho\mathbf{u}\cdot\mathbf{F}\,dV$ after applying the divergence theorem. Assuming a 1.5-layer setting, that is, ignoring the energy above the lower layer, and denoting the upper and lower layers with subscripts 1 and 2, respectively, the energy loss integrated between two cross sections east and west of the sill is inferred from the energy flux $\rho_2 Q\Delta B$ across those sections (Freeland and Farmer 1980). Assuming homogeneous, incompressible, and irrotational flow, the Bernoulli function $B$ of the active lower layer is $\rho_2 B = (1/2)\rho_2 u_2^2 + \rho_1 gH + \Delta\rho g h_2$ (Nash and Moum 2001), where $H$ and $h_2$ are the total and lower-layer depths, respectively, and $\Delta\rho$ is the in situ density difference between the two layers. The difference of the Bernoulli function at two cross-canyon sections $\Delta B$ is estimated from individual profiles east and west of the sill (Fig. 4a). In the absence of velocity measurements from both sides of the sill unaffected by tidal and near-inertial features, the cross-section area provides the eastward velocity of each section, assuming a constant transport $Q$ around the sill of 0.1 Sv in the lower layer as measured by P1. Alternative estimates based on an assumption of constant velocity give similar results. The 2-layer interface at 28.13 deepens from 3850 to 3895 m across the sill. Additionally, the mean lower-layer density $\rho_2$ reduces from 28.17 to 28.15 (Fig. 4a) across the sill. The lower-layer energy loss around the sill accounts for 24.9 MW, which represents mostly the loss of potential energy given the scales of the first and last terms of $\rho_2 Q\Delta B$ of $\sim 10^3$ and $\sim 10^7\,\mathrm{kg\,m^2\,s^{-1}}$, respectively. The averaged dissipation rate $1.0\times10^{-9}\,\mathrm{W\,kg^{-1}}$ volume integrated above the sill $\int\rho(\varepsilon + J_b)\,dV$, in contrast, only accounts for 0.05 MW of energy loss, when assuming a constant turbulent buoyancy flux $J_b = 0.2\varepsilon$ responsible for the increase in potential energy.

In addition, the frictional boundary layer affects through the bottom stress $\tau_0$ the energy of the lower layer differently over the sill, where higher bottom velocities are noticed, than within the canyon away from the sill. This effect is evaluated from CTD/LADCP profiles in the sill passage, assuming a layer of constant stress defined by the bottom stress $\tau_0$ with $\tau_0 = \rho u_*^2$. The friction velocity $u_*$ is calculated from the law of the wall for the velocity $U$ in the boundary layer (Dewey and Crawford 1988): $U = (u_*/\kappa)\ln(z/z_0)$. The bottom boundary layer thickness of 127–133 m in the sill passage is estimated from the density difference of $0.002\,\mathrm{kg\,m^{-3}}$ relative to the bottom density. Because of the reduced bottom stratification observed deeper than 4400 m (Fig. 4), this layer thickness decreases above the sill but remains present within the sill passage. A linear least squares fit of the velocity versus the logarithm of the height above bottom $\ln(z)$ allows us to estimate the friction velocity for an undefined $z_0$ with a von Kármán constant $\kappa$ of 0.4. The friction velocity is $0.003\,\mathrm{m\,s^{-1}}$, providing a bottom stress of 0.0075 Pa. Using the maximal velocity of $0.3\,\mathrm{m\,s^{-1}}$ (Fig. 3), the integrated bottom boundary energy loss $\int_A u\tau_0\,dA$ ($A = 19\,\mathrm{km}\times 8\,\mathrm{km}$, the along and across sill lengths, respectively) becomes 0.3 MW, substantially below the drop in Bernoulli function.

The contribution of the spatially integrated measured dissipation rate with the frictional boundary layer estimate accounts for 2% of the lower-layer energy loss. This underlines that high dissipation may have been undersampled or that additional mechanisms may play a substantial role near the sill, such as horizontal eddy shedding around the three-dimensional topography (MacCready and Pawlak 2001). As noticed over a different sill (Klymak and Gregg 2004), the radiated energy by internal waves can account for a significant fraction of the barotropic energy loss when the measured dissipation rate remains low in comparison to the Bernoulli drop. In the deep fracture zone over the sill, internal waves may not only be generated by the barotropic tides but also by the steady-state overflow and participate in the drop in the Bernoulli function. The tidal advection across the sill may, however, hinder a clear distinction between those waves.

### b. Internal wave radiation

We evaluate the internal wave energy flux around the sill from the wave characteristics measured at P1. In the narrow sill passage, the tidal excursion length $U/\omega_{M_2}$ of 0.7–1.4 km (using $U = 0.1$–$0.2\,\mathrm{m\,s^{-1}}$) is smaller than the sill width of 8 km. The streamwise slope of the sill is $\alpha = 1/10$, that is, subcritical for $M_2$ tidal rays (1/8 slope). In this regime, internal tides are expected to radiate energy upward away from the sill both down and up canyon at the fundamental frequency, as predicted by the acoustic limit from the model of Bell (1975). The vertical and horizontal wave energy fluxes $c_{gz}E$ and $c_{gh}E$ are estimated from the group velocities $c_{gz}$ and $c_{gh}$ and from the total energy density $E = E_{KE} + E_{PE}$. Assuming a 2D wave generation across the sill, both the vertical $m$ and horizontal $\kappa_h$ wavenumbers are needed to estimate the group velocities $c_{gz} = -(\omega^2 - f^2)^{3/2}/(\omega N \kappa_h)$ and $c_{gh} = N(\omega^2 - f^2)^{1/2}/(\omega m)$ in the rotating wave regime with $\omega$ of the order of $f$ but $\omega \geq f$ (Gill 1982). The prevalence of upward-propagating energy associated with the semidiurnal shear occurs for vertical wavelengths from 90 m up to at least 560 m (Fig. 12) limited by the MMP range. The corresponding horizontal wavelength range $\kappa_h$ of 5.2–32.3 km is inferred from the internal wave dispersion relation $\kappa_h/m = (\omega^2 - f^2)/(N^2 - \omega^2)$. Those wavelength ranges, used subsequently for the internal tide energy fluxes, produce vertical and horizontal group velocities of 1.3–8.1 and $1.3$–$8.3\,\mathrm{cm\,s^{-1}}$, respectively.

To estimate the total energy phased locked with semidiurnal tides, we select the velocity of $0.05\,\mathrm{m\,s^{-1}}$ and the buoyancy frequency of $0.9 \times 10^{-3}\,\mathrm{s^{-1}}$ depth averaged around the 2-layer interface at westward tidal flow (Fig. 10). Amplitudes of isopycnal displacements of 50 m are selected in a similar manner through the $M_2$ cycle. The total energy density $E$ becomes $3.6\,\mathrm{J\,m^{-3}}$, which yields vertical and horizontal energy fluxes of 0.05–0.29 and $0.05$–$0.30\,\mathrm{W\,m^{-2}}$, respectively. The total flux, that is, the sum of the vertical flux integrated horizontally across the overflow area (3.4 km × 19 km; 3.4 km is the across-sill width that encompasses the largest isopycnal displacements in Fig. 8a) and the horizontal fluxes integrated across the two cross-canyon sections (both S = 0.6 km × 19 km), is 4.1–25.8 MW. The energy radiated away by internal tides is comparable to the lower-layer energy loss.

In addition, the linear theory of internal tides and lee waves (Gill 1982) predicts a vertical energy flux $F_z = (1/2)\rho_0[(N^2 - U^2k^2)(U^2k^2 - f^2)]^{1/2}Uh_0^2$ of $0.25$–$0.61\,\mathrm{W\,m^{-2}}$ with $h_0$ as the blocking depth (100–200 m) and $k$ as the cross-sill extent ($h_0/\alpha$). The vertical flux integrated across the overflow area of 17.1–41.4 MW compares with the total energy flux observed around the sill. This further suggests the substantial role played by internal waves in the overflow region and confirms the importance of both representing the canyon and the sill topography to evaluate the energy dissipation of the barotropic tides and of the mean lower-layer flow.

## 5. Conclusions

We carried out an analysis of data collected during the DoMORE project in one of the many fracture zone canyons corrugating the western flank of the MAR in the South Atlantic. The primary results emphasize the effects of a variety of mechanisms affecting the turbulent mixing of deep water in the canyon:

- A deep 2-layer exchange mean flow transports 0.04–0.10 Sv of AABW eastward in the deepest layer, which is laterally confined by the canyon walls below ~3900 m.
- The along-canyon density gradient reaches a maximum in a region where a tall abyssal hill restricts the canyon both laterally (constriction) and vertically (sill) and where the mean lower-layer velocity is larger ($5.2\,\mathrm{cm\,s^{-1}}$) than ≈100 km east of the sill ($1.8\,\mathrm{cm\,s^{-1}}$). The semidiurnal tides are not strong enough to reverse the entire lower layer, indicating that the overflow acts like a check valve for up-canyon flow below ≈4000 m.
- Consistent with the hypothesis of a tidally modulated, hydraulically controlled overflow, the largest dissipation rate $\varepsilon \approx 10^{-7}\,\mathrm{W\,kg^{-1}}$ and diapycnal diffusivity $\kappa \approx 10^{-3}\,\mathrm{m^2\,s^{-1}}$ were observed east of the sill crest below 3500 m. The isopycnal rebound east of the sill is reminiscent of a hydraulic jump.
- Large overturns in the sill passage (P1) occur primarily during westward semidiurnal tidal flow. Those overturns, intensified around 3800–4000 m, relate to the reduced stratification observed at the sill during westward tides.
- Internal tides with upward-propagating energy are generated specially in the vicinity of the sill. In contrast, at the downstream mooring site (P3), the internal wave field is dominated by near-inertial waves with downward-propagating energy.

The DoMORE data confirm the existence of a lower layer flowing zonally toward the MAR in the BBTRE canyon (St. Laurent et al. 2001a; Thurnherr et al. 2005). Similar up-canyon currents toward the ridge crest were inferred for many other canyons in the western South Atlantic (Mercier et al. 2000; Thurnherr and Speer 2003). Since abyssal hills are intrinsically associated with seafloor spreading, similar dynamics with elevated turbulence and mixing occurring primarily

near tidally modulated overflows are expected to occur in many of the FZ canyons corrugating the global slow-spreading midocean ridge system. If each FZ canyon hosts one major sill comparable to the one described above, ≈1.3 GW of energy is dissipated in the ≈40 canyons of the Brazil Basin (Thurnherr et al. 2005). This number can be compared with the 2.7–4.8 GW of energy dissipated in the Strait of Gibraltar (Wesson and Gregg 1994) in a region of remarkably high dissipation rate.

*Acknowledgments.* The DoMORE project was supported by NSF under the Grant OCE-1235094. The author thanks J. M. Toole for his assistance in the processing of MMPs and J. R. Ledwell for commenting the manuscript. Suggestions by two anonymous reviewers greatly improved the manuscript. The effort of J. Zhao and of colleagues from LDEO, WHOI, and the crew of the R/V *Nathaniel B. Palmer* was greatly appreciated prior and during the two DoMORE cruises.

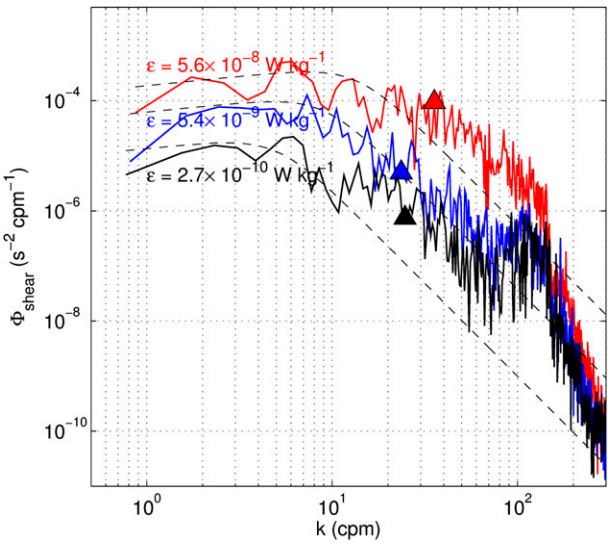


FIG. A1. Microstructure shear spectra of one DMP profile (vad005) averaged over the two probes taken for three depth bins at 21.08°S and 14.64°W. The black dashed lines represent the universal velocity shear spectra inferred from the Nasmyth (1970) spectra. The upper-wavenumber limit is denoted by the triangle.

## APPENDIX A

### Dissipation Rate from Deep Microstructure Profiler

The methodology for computing the dissipation rate from airfoils has a long history that is described in detail in the literature; Lueck et al. (2002) give a comprehensive review. Considerable details of the analysis methodologies are described by the Rockland Scientific Technical Note 28 (available online at http://www.rocklandscientific.com). A contemporary innovation involves the concurrent use of high-frequency motion sensing through multiaxis analog accelerometers. Using cospectral analysis, we remove the platform-induced vibrations from the probe records using the method of Goodman et al. (2006). Typically, this correction applies to frequencies between about 10 and 60 Hz. In the resulting "clean" shear spectra, coherent vibrational energy between the profiler platform and the shear records has been removed. For the RVMP system, this allows us to measure dissipation rates as low as about 3–5 $\times$ $10^{-11}$ W kg$^{-1}$ (Fig. A1).

To estimate the dissipation rate from the cleaned spectra, we follow the spectral analysis procedure described by Gregg (1999). In practice, the microstructure records were examined in 2048-element windows over which a 1024-element FFT was employed. Adjacent 1024-element bins are treated using a Hanning window employed with 50% overlap. For the typical fall speed of 0.75 m s$^{-1}$, this results in spectral variance estimates at 1.5-m depth intervals of each microstructure shear record. The limits of integration are taken from the lowest wavenumber to an upper-wavenumber cutoff calculated as either 100 cpm or a lesser wavenumber representing the transition between the dissipative subrange and the blue portion of the high-wavenumber spectrum dominated by electronic noise. In practice, the noise-limited wavenumber nearly always applies. This cutoff wavenumber is found through identifying the corresponding root of the fifth-order polynomial fit to the spectral curve. No corrections are applied to the shear spectra, as the inertial subrange and dissipative rolloff are always well resolved in these data. Dual shear probes were always used and the dissipation rate reported is typically the mean of the independently estimated dissipation rates from each probe signal.

As a measure of fidelity, each spectrum is compared to the canonical spectral form derived by Nasmyth (1970) for the calculated value of the dissipation rate. Measured spectra generally show good agreement with Nasmyth (Fig. A1). In cases where the measured spectra deviate substantially, we flag them as suspect and do not include them in the dissipation estimates. In the final analysis where we combine the CTD data with the dissipation estimates, we compute the Ozmidov wavenumber as $(N^3/\varepsilon)^{1/2}$ (Thorpe 1977). As the Ozmidov wavenumber corresponds to the lowest wavenumber for the dissipation integral, we reexamine the dissipation estimate by integrating each Nasmyth spectra from its associated Ozmidov wavenumber to infinity. This allows

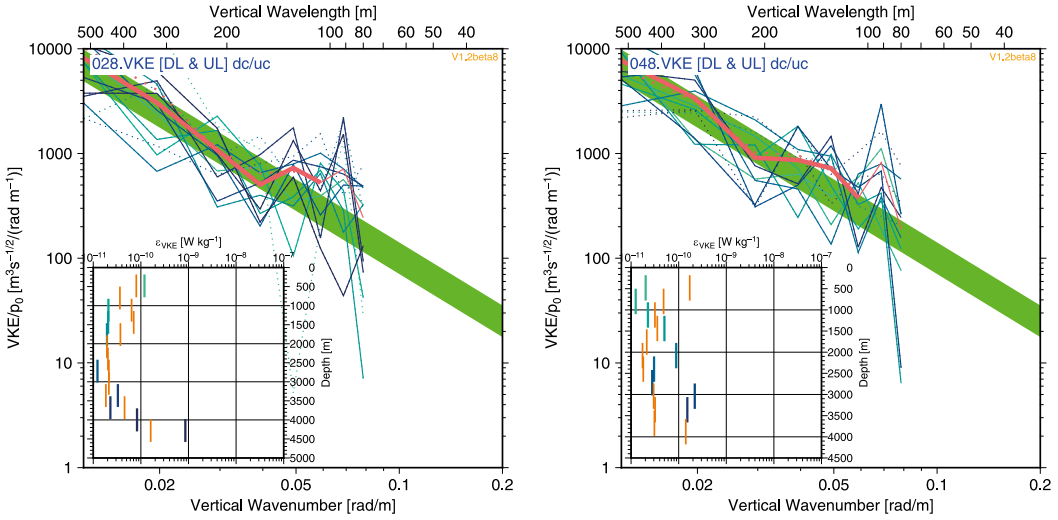


FIG. B1. VKE finestructure parameterization diagnostic plots from two profiles with available microstructure data. The insets show the VKE-derived dissipation profiles in blue and the identically averaged corresponding microstructure data in orange. The main panels show the corresponding normalized VKE spectra in the same shades of blue used in the inset; no $\varepsilon_{\mathrm{VKE}}$ estimates are produced for the dotted spectra, which fail one or more of the consistency checks built into the processing software. The station-averaged VKE spectra are shown in salmon color with a thicker line in the finescale range used for the spectral fits; the green band shows the empirical VKE spectrum with a factor of 2 uncertainty. (left) Example profile 28 with strong bottom-intensified turbulence. (right) Example profile 48 with low turbulence levels throughout the water column.

us to examine the uncertainty caused by missing variance in the data spectral estimates, both at the lower and upper ends of the spectrum. We flag cases where the resulting estimate of integrated variance differs by more than 10% from the data estimate. These cases represent less than 0.1% of all estimates and are not included in further estimates.

## APPENDIX B

### Vertical Kinetic Energy Finestructure Parameterization Method for TKE Dissipation

Turbulence measurements with free-falling microstructure profilers are expensive and time consuming to collect. Since there is a close relationship between internal waves and turbulence, it has become common practice to estimate turbulence and mixing levels with ''finestructure parameterization methods'' from internal wave signals measured with standard oceanographic CTDs and ADCPs (Kunze et al. 2006). Here, we use a recently developed method that is based on LADCP-derived vertical kinetic energy (Thurnherr et al. 2015) to elucidate spatial and temporal patterns of turbulence along the BBTRE canyon (Fig. 2). The VKE method is empirical and has been found to yield estimates consistent within a factor of 2 with simultaneous microstructure measurements in a suite of datasets taken between 10° and 70° of latitude and that include both Luzon Strait, a region of extreme internal wave activity, and the open South Pacific, where internal waves and turbulence levels are considered oceanic background. Importantly, there are no indications of significant biases of the VKE method applied in regions of internal wave generation; that is, the method is expected to work well in the BBTRE canyon. Consistent with this inference, individual profiles of microstructure and VKE-derived dissipation in the DoMORE-2 data are generally similar, although the errors associated with the individual VKE samples can exceed a factor of 5 (insets in Fig. B1). A scatterplot of VKE- versus microstructure-derived $\varepsilon$ indicates agreement within a factor of 2 when suitably averaged, in agreement with Fig. 2 of Thurnherr et al. (2015), and the corresponding dataset-averaged mean profiles are also mutually consistent within a factor of 2 throughout the water column (not shown).

The VKE parameterization method is based on the observation that vertical wavenumber $m$ finestructure spectra of vertical ocean velocity have a universal $m^{-2}$ slope that, in contrast to the Garrett–Munk model, does not vary with latitude, density stratification, or the bandwidth of the internal wave field but only with local turbulence levels (Thurnherr et al. 2015). This power law usually holds on vertical scales between a low

wavelength cutoff, which varies with the VKE energy level and LADCP data quality but which is typically around 100 m and usually extends to vertical scales in excess of 500 m. The quality of the parameterization estimates depends primarily on how well the empirical $m^{-2}$ spectrum can be fit to the observations. Most of the individual DoMORE-2 VKE spectra are consistent with an $m^{-2}$ power law on vertical wavelengths below 500 m down to vertical scales between 100 and 200 m (Fig. B1, main panels). On shorter wavelengths, LADCP measurement noise becomes significant and flattens the spectra.

## REFERENCES


Alford, M. H., J. B. Girton, G. Voet, G. S. Carter, J. B. Mickett, and J. M. Klymak, 2013: Turbulent mixing and hydraulic control of abyssal water in the Samoan Passage. *Geophys. Res. Lett.*, **40**, 4668–4674, doi:10.1002/grl.50684.

Arneborg, L., and B. Liljebladh, 2009: Overturning and dissipation caused by baroclinic tidal flow near the sill of a fjord basin. *J. Phys. Oceanogr.*, **39**, 2156–2174, doi:10.1175/2009JPO4037.1.

Baines, B. G., 1995: *Topographic Effects in Stratified Flows.* Cambridge University Press, 500 pp.

Bell, T. H., 1975: Lee waves in stratified flows with simple harmonic time dependence. *J. Fluid Mech.*, **67**, 705–722, doi:10.1017/S0022112075000560.

Carter, G. S., and M. C. Gregg, 2002: Intense variable mixing near the head of Monterey Submarine Canyon. *J. Phys. Oceanogr.*, **32**, 3145–3165, doi:10.1175/1520-0485(2002)032<3145:IVMNTH>2.0.CO;2.

Clément, L., E. Frajka-Williams, Z. B. Szuts, and S. A. Cunningham, 2014: Vertical structure of eddies and Rossby waves, and their effect on the Atlantic meridional overturning circulation at 26.5°N. *J. Geophys. Res. Oceans*, **119**, 6479–6498, doi:10.1002/2014JC010146.

Dewey, R. K., and W. R. Crawford, 1988: Bottom stress estimates from vertical dissipation rate profiles on the continental shelf. *J. Phys. Oceanogr.*, **18**, 1167–1177, doi:10.1175/1520-0485(1988)018<1167:BSEFVD>2.0.CO;2.

Dillon, T. M., 1982: Vertical overturns: A comparison of Thorpe and Ozmidov length scales. *J. Geophys. Res.*, **87**, 9601–9613, doi:10.1029/JC087iC12p09601.

Doherty, K. W., D. E. Frye, S. P. Liberatore, and J. M. Toole, 1999: A moored profiling instrument. *J. Atmos. Oceanic Technol.*, **16**, 1816–1829, doi:10.1175/1520-0426(1999)016<1816:AMPI>2.0.CO;2.

Egbert, G. D., and S. Y. Erofeeva, 2002: Efficient inverse modeling of barotropic ocean tides. *J. Phys. Oceanogr.*, **19**, 183–204, doi:10.1175/1520-0426(2002)019<0183:EIMOBO>2.0.CO;2.

Farmer, D. M., and J. D. Smith, 1980: Tidal interaction of stratified flow with a sill in Knight Inlet. *Deep-Sea Res.*, **27A**, 239–254, doi:10.1016/0198-0149(80)90015-1.

Ferron, B., H. Mercier, K. Speer, A. Gargett, and K. Polzin, 1998: Mixing in the Romanche Fracture Zone. *J. Phys. Oceanogr.*, **28**, 1929–1945, doi:10.1175/1520-0485(1998)028<1929:MITRFZ>2.0.CO;2.

Freeland, H. J., and D. M. Farmer, 1980: Circulation and energetics of a deep, strongly stratified inlet. *Can. J. Fish. Aquat. Sci.*, **37**, 1398–1410, doi:10.1139/f80-179.

Galbraith, P. S., and D. E. Kelley, 1996: Identifying overturns in CTD profiles. *J. Atmos. Oceanic Technol.*, **13**, 688–702, doi:10.1175/1520-0426(1996)013<0688:IOICP>2.0.CO;2.

Gargett, A., and T. Garner, 2008: Determining Thorpe scales from ship-lowered CTD density profiles. *J. Atmos. Oceanic Technol.*, **25**, 1657–1670, doi:10.1175/2008JTECHO541.1.

Gill, A. E., 1982: *Atmosphere–Ocean Dynamics.* Academic Press, 662 pp.

Goodman, L., E. R. Levine, and R. Lueck, 2006: On measuring the terms of the turbulent kinetic energy budget from an AUV. *J. Atmos. Oceanic Technol.*, **23**, 977–990, doi:10.1175/JTECH1889.1.

Gordon, R. L., and N. F. Marshall, 1976: Submarine canyons: Internal wave traps? *Geophys. Res. Lett.*, **3**, 622–624, doi:10.1029/GL003i010p00622.

Gregg, M. C., 1989: Scaling turbulent dissipation in the thermocline. *J. Geophys. Res.*, **94**, 9686–9698, doi:10.1029/JC094iC07p09686.

——, 1999: Uncertainties and limitations in measuring $\epsilon$ and $\chi_T$. *J. Atmos. Oceanic Technol.*, **16**, 1483–1490, doi:10.1175/1520-0426(1999)016<1483:UALIMA>2.0.CO;2.

Hinze, J. O., 1975: *Turbulence*. 2nd ed. McGraw-Hill, 790 pp.

Hogg, N. G., and W. B. Owens, 1999: Direct measurement of the deep circulation within the Brazil Basin. *Deep-Sea Res. II*, **46**, 335–353, doi:10.1016/S0967-0645(98)00097-6.

——, ——, G. Siedler, and W. Zenk, 1996: Circulation in the deep Brazil Basin. *The South Atlantic: Present and Past Circulation*, G. Wefer et al., Eds., Springer, 249–260.

Hotchkiss, F. S., and C. Wunsch, 1982: Internal waves in Hudson Canyon with possible geological implications. *Deep-Sea Res.*, **29**, 415–442, doi:10.1016/0198-0149(82)90068-1.

Jackett, D. R., and T. J. McDougall, 1997: A neutral density variable for the world's oceans. *J. Phys. Oceanogr.*, **27**, 237–263, doi:10.1175/1520-0485(1997)027<0237:ANDVFT>2.0.CO;2.

Kinder, T. H., and H. L. Bryden, 1990: The aspiration of deep waters through straits. *The Physical Oceanography of Sea Straits*, L. J. Pratt, Ed., Kluwer Academic, 295–319.

Klymak, J. M., and M. C. Gregg, 2004: Tidally generated turbulence over the Knight Inlet sill. *J. Phys. Oceanogr.*, **34**, 1135–1151, doi:10.1175/1520-0485(2004)034<1135:TGTOTK>2.0.CO;2.

Koop, C. G., and B. McGee, 1986: Measurements of internal gravity waves in a continuously stratified shear flow. *J. Fluid Mech.*, **172**, 453–480, doi:10.1017/S0022112086001817.

Kunze, E., M. G. Briscoe, and A. J. Williams III, 1990a: Interpreting shear and strain fine structure from a neutrally buoyant float. *J. Geophys. Res.*, **95**, 18 111–18 125, doi:10.1029/JC095iC10p18111.

——, A. J. Williams III, and M. G. Briscoe, 1990b: Observations of shear and vertical stability from a neutrally buoyant float. *J. Geophys. Res.*, **95**, 18 127–18 142, doi:10.1029/JC095iC10p18127.

——, L. K. Rosenfeld, G. S. Carter, and M. C. Gregg, 2002: Internal waves in Monterey Submarine Canyon. *J. Phys. Oceanogr.*, **32**, 1890–1913, doi:10.1175/1520-0485(2002)032<1890:IWIMSC>2.0.CO;2.

——, E. Firing, J. M. Hummon, T. K. Chereskin, and A. M. Thurnherr, 2006: Global abyssal mixing inferred from lowered ADCP shear and CTD strain profiles. *J. Phys. Oceanogr.*, **36**, 1553–1576, doi:10.1175/JPO2926.1.

Leaman, K. D., and T. B. Sanford, 1975: Vertical energy propagation of inertial waves: A vector spectral analysis of velocity profiles. *J. Geophys. Res.*, **80**, 1975–1978, doi:10.1029/JC080i015p01975.

Ledwell, J. R., T. Donoghue, B. Guest, P. Lemmond, C. Sellers, and N. Cortes, 2000a: Cruise report: R/V *Knorr* cruise 161-6: 7 April to 16 May 2000: Brazil Basin Tracer Release Experiment. WHOI Cruise Rep., 41 pp.

——, E. T. Montgomery, K. L. Polzin, L. C. St. Laurent, R. W. Schmitt, and J. M. Toole, 2000b: Evidence for enhanced mixing over rough topography in the abyssal ocean. *Nature*, **403**, 179–182, doi:10.1038/35003164.

Lueck, R. G., F. Wolk, and H. Yamazaki, 2002: Oceanic velocity microstructure measurements in the 20th century. *J. Oceanogr.*, **58**, 153–174, doi:10.1023/A:1015837020019.

MacCready, P., and G. Pawlak, 2001: Stratified flow along a corrugated slope: Separation drag and wave drag. *J. Phys. Oceanogr.*, **31**, 2824–2839, doi:10.1175/1520-0485(2001)031<2824:SFAACS>2.0.CO;2.

MacKinnon, J. A., T. M. S. Johnston, and R. Pinkel, 2008: Strong transport and mixing of deep water through the Southwest Indian Ridge. *Nat. Geosci.*, **1**, 755–758, doi:10.1038/ngeo340.

Mater, B. D., S. K. Venayagamoorthy, L. C. St. Laurent, and J. N. Moum, 2015: Biases in Thorpe scale estimates of turbulence dissipation. Part I: Assessments from large-scale overturns in oceanographic data. *J. Phys. Oceanogr.*, **45**, 2497–2521, doi:10.1175/JPO-D-14-0128.1.

Mercier, H., and P. Morin, 1997: Hydrography of the Romanche and Chain Fracture Zones. *J. Geophys. Res.*, **102**, 10 373–10 389, doi:10.1029/97JC00229.

——, G. L. Weatherly, and M. Arhan, 2000: Bottom water throughflows at the Rio de Janeiro and Rio Grande Fracture Zones. *Geophys. Res. Lett.*, **27**, 1503–1506, doi:10.1029/2000GL011402.

Miles, J. W., and L. N. Howard, 1964: Note on a heterogeneous shear flow. *J. Fluid Mech.*, **20**, 331–336, doi:10.1017/S0022112064001252.

Mudge, T., and R. G. Lueck, 1994: Digital signal processing to enhance oceanographic observations. *J. Atmos. Oceanic Technol.*, **11**, 825–836, doi:10.1175/1520-0426(1994)011<0825:DSPTEO>2.0.CO;2.

Munk, W., 1966: Abyssal recipes. *Deep-Sea Res. Oceanogr. Abstr.*, **13**, 707–730, doi:10.1016/0011-7471(66)90602-4.

Nash, J. D., and J. N. Moum, 2001: Internal hydraulic flows on the continental shelf: High drag states over a small bank. *J. Geophys. Res.*, **106**, 4593–4612, doi:10.1029/1999JC000183.

Nasmyth, P. W., 1970: Ocean turbulence. Ph.D. thesis, University of British Columbia, 69 pp.

Osborn, T. R., 1980: Estimates of the local rate of vertical diffusion from dissipation estimates. *J. Phys. Oceanogr.*, **10**, 83–89, doi:10.1175/1520-0485(1980)010<0083:EOTLRO>2.0.CO;2.

Pawlowicz, R., B. Beardsley, and S. Lentz, 2002: Classical tidal harmonic analysis including error estimates in MATLAB using T_TIDE. *Comput. Geosci.*, **28**, 929–937, doi:10.1016/S0098-3004(02)00013-4.

Polzin, K. L., J. M. Toole, and R. W. Schmitt, 1995: Finescale parameterizations of turbulent dissipation. *J. Phys. Oceanogr.*, **25**, 306–328, doi:10.1175/1520-0485(1995)025<0306:FPOTD>2.0.CO;2.

——, K. G. Speer, J. M. Toole, and R. W. Schmitt, 1996: Intense mixing of Antarctic Bottom Water in the equatorial Atlantic Ocean. *Nature*, **380**, 54–57, doi:10.1038/380054a0.

——, J. M. Toole, J. R. Ledwell, and R. W. Smith, 1997: Spatial variability of turbulent mixing in the abyssal ocean. *Science*, **276**, 93–96, doi:10.1126/science.276.5309.93.

Purkey, S. G., and G. C. Johnson, 2010: Warming of global abyssal and deep Southern Ocean waters between the 1990s and 2000s: Contributions to global heat and sea level rise budgets. *J. Climate*, **23**, 6336–6351, doi:10.1175/2010JCLI3682.1.

Staalstrøm, A., L. Arneborg, B. Liljebladh, and G. Broström, 2015: Observations of turbulence caused by a combination of tides and mean baroclinic flow over a fjord sill. *J. Phys. Oceanogr.*, **45**, 355–368, doi:10.1175/JPO-D-13-0200.1.

St. Laurent, L. C., and C. Garrett, 2002: The role of internal tides in mixing the deep ocean. *J. Phys. Oceanogr.*, **32**, 2882–2899, doi:10.1175/1520-0485(2002)032<2882:TROITI>2.0.CO;2.

——, and A. M. Thurnherr, 2007: Intense mixing of lower thermocline water on the crest of the Mid-Atlantic Ridge. *Nature*, **448**, 680–683, doi:10.1038/nature06043.

——, J. M. Toole, and R. W. Schmitt, 2001a: Buoyancy forcing by turbulence above rough topography in the abyssal Brazil Basin. *J. Phys. Oceanogr.*, **31**, 3476–3495, doi:10.1175/1520-0485(2001)031<3476:BFBTAR>2.0.CO;2.

——, ——, and ——, 2001b: Mixing and diapycnal advection in the ocean. *From Stirring to Mixing in a Stratified Ocean: Proc. 'Aha Huliko'a Hawaiian Winter Workshop*, Honolulu, HI, University of Hawai'i at Mānoa, 175–185.

Stommel, H., and A. B. Arons, 1960: On the abyssal circulation of the World Ocean—I. Stationary planetary flow patterns on a sphere. *Deep-Sea Res.*, **6**, 140–154, doi:10.1016/0146-6313(59)90065-6.

——, ——, and A. J. Faller, 1958: Some examples of stationary planetary flow patterns in bounded basins. *Tellus*, **10A**, 179–187, doi:10.1111/j.2153-3490.1958.tb02003.x.

Talley, L. D., 2013: Closure of the global overturning circulation through the Indian, Pacific, and Southern Oceans: Schematics and transports. *Oceanography*, **26**, 80–97, doi:10.5670/oceanog.2013.07.

Thomson, R. E., and W. J. Emery, 2014: *Data Analysis Methods in Physical Oceanography.* 3rd ed. Elsevier, 728 pp.

Thorpe, S. A., 1977: Turbulence and mixing in a Scottish loch. *Philos. Trans. Roy. Soc. London*, **A286**, 125–181, doi:10.1098/rsta.1977.0112.

Thurnherr, A. M., 2011: Vertical velocity from LADCP data. *10th Current, Waves and Turbulence Measurements (CWTM)*, Monterey, CA, IEEE, 198–204, doi:10.1109/CWTM.2011.5759552.

——, and K. J. Richards, 2001: Hydrography and high-temperature heat flux of the Rainbow hydrothermal site (36°14′N, Mid-Atlantic Ridge). *J. Geophys. Res.*, **106**, 9411–9426, doi:10.1029/2000JC900164.

——, and K. G. Speer, 2003: Boundary mixing and topographic blocking on the Mid-Atlantic Ridge in the South Atlantic. *J. Phys. Oceanogr.*, **33**, 848–862, doi:10.1175/1520-0485(2003)33<848:BMATBO>2.0.CO;2.

——, and ——, 2004: Representativeness of meridional hydrographic sections in the western South Atlantic. *J. Mar. Res.*, **62**, 37–65, doi:10.1357/00222400460744618.

——, K. J. Richards, C. R. German, G. F. Lane-Serff, and K. G. Speer, 2002: Flow and mixing in the rift valley of the Mid-Atlantic Ridge. *J. Phys. Oceanogr.*, **32**, 1763–1778, doi:10.1175/1520-0485(2002)032<1763:FAMITR>2.0.CO;2.

——, L. C. St. Laurent, K. G. Speer, J. M. Toole, and J. R. Ledwell, 2005: Mixing associated with sills in a canyon on the mid-ocean ridge flank. *J. Phys. Oceanogr.*, **35**, 1370–1381, doi:10.1175/JPO2773.1.

——, G. Reverdin, P. Bouruet-Aubertot, L. St. Laurent, A. Vangriesheim, and V. Ballu, 2008: Hydrography and flow in the Lucky Strike segment of the Mid-Atlantic Ridge. *J. Mar. Res.*, **66**, 347–372, doi:10.1357/002224008786176034.

——, E. Kunze, J. M. Toole, L. St. Laurent, K. J. Richards, and A. Ruiz-Angulo, 2015: Vertical kinetic energy and turbulent dissipation in the ocean. *Geophys. Res. Lett.*, **42**, 7639–7647, doi:10.1002/2015GL065043.

Tippenhauer, S., M. Dengler, T. Fischer, and T. Kanzow, 2015: Turbulence and finestructure in a deep ocean channel with sill overflow on the Mid-Atlantic Ridge. *Deep-Sea Res. I*, **99**, 10–22, doi:10.1016/j.dsr.2015.01.001.

Toole, J. M., 2007: Temporal characteristics of abyssal finescale motions above rough bathymetry. *J. Phys. Oceanogr.*, **37**, 409–427, doi:10.1175/JPO2988.1.

——, K. W. Doherty, D. E. Frye, and S. P. Liberatore, 1999: Velocity measurements from a moored profiling instrument. *Proc. Sixth Working Conf. on Current Measurement*, San Diego, CA, IEEE, 144–149.

Tucholke, B. E., and J. Lin, 1994: A geological model of the structure of ridge segments in the slow spreading ocean crust. *J. Geophys. Res.*, **99**, 11 937–11 958, doi:10.1029/94JB00338.

Turner, J. S., 1973: *Buoyancy Effects in Fluids.* Cambridge University Press, 367 pp.

Visbeck, M., 2002: Deep velocity profiling using lowered acoustic Doppler current profilers: Bottom track and inverse solutions. *J. Atmos. Oceanic Technol.*, **19**, 794–807, doi:10.1175/1520-0426(2002)019<0794:DVPULA>2.0.CO;2.

Voet, G., J. B. Girton, M. H. Alford, G. S. Carter, J. M. Klymak, and J. B. Mickett, 2015: Pathways, volume transport, and mixing of abyssal water in the Samoan Passage. *J. Phys. Oceanogr.*, **45**, 562–588, doi:10.1175/JPO-D-14-0096.1.

Waterman, S., A. C. Naveira Garabato, and K. L. Polzin, 2013: Internal waves and turbulence in the Antarctic Circumpolar Current. *J. Phys. Oceanogr.*, **43**, 259–282, doi:10.1175/JPO-D-11-0194.1.

Wesson, J. C., and M. C. Gregg, 1994: Mixing at Camarinal Sill in the Strait of Gibraltar. *J. Geophys. Res.*, **99**, 9847–9878, doi:10.1029/94JC00256.

Whitehead, J. A., 1998: Topographic control of oceanic flows in deep passages and straits. *Rev. Geophys.*, **36**, 423–440, doi:10.1029/98RG01014.

——, A. Leetma, and R. A. Knox, 1974: Rotating hydraulics of strait and sill flows. *Geophys. Fluid Dyn.*, **6**, 101–125, doi:10.1080/03091927409365790.

Wijesekera, H. W., T. M. Dillon, and L. Padman, 1993: Some statistical and dynamical properties of turbulence in the oceanic pycnocline. *J. Geophys. Res.*, **98**, 22 665–22 679, doi:10.1029/93JC02352.